OXFORD

Human Molecular Genetics, 2023, Vol. 32, 2, 333–350
https://doi.org/10.1093/hmg/ddac201
Advance access publication date 22 August 2022
Original Article

Mitofusin 2 mutation drives cell proliferation in Charcot-Marie-Tooth 2A fibroblasts

Paola Zanfardino[1,†], Giovanna Longo[1,†,‡], Alessandro Amati[1], Federica Morani[2], Ernesto Picardi[3,4], Francesco Girolamo[1], Mariella Pafundi[1], Sharon N. Cox[3], Caterina Manzari[3], Apollonia Tullo[4], Stefano Doccini[5], Filippo M. Santorelli[5] and Vittoria Petruzzella[1,*]

[1]Department of Medical Basic Sciences, Neurosciences and Sense Organs, University of Bari Aldo Moro, 70124 Bari, Italy
[2]Department of Biology, University of Pisa, 56126 Pisa, Italy
[3]Department of Biosciences, Biotechnology and Biopharmaceutics, University of Bari, 70125 Bari, Italy
[4]Institute of Biomembranes, Bioenergetics and Molecular Biotechnologies, National Research Council, 70125 Bari, Italy
[5]Molecular Medicine for Neurodegenerative and Neuromuscular Diseases Unit, IRCCS Fondazione Stella Maris, 56128 Pisa, Italy
*To whom correspondence should be addressed at: Department of Medical Basic Sciences, Neurosciences and Sense Organs, University of Bari Aldo Moro, Piazza G. Cesare, 11, 70124 Bari, Italy. Tel: +39 080 5448530; Fax +39 080 5448528; Email: vittoria.petruzzella@uniba.it
†These authors contributed equally.
‡Present address: Institute of Biomembranes, Bioenergetics and Molecular Biotechnologies, National Research Council, 70125 Bari, Italy.

Abstract

Dominant mutations in ubiquitously expressed mitofusin 2 gene (*MFN2*) cause Charcot-Marie-Tooth type 2A (CMT2A; OMIM 609260), an inherited sensory-motor neuropathy that affects peripheral nerve axons. Mitofusin 2 protein has been found to take part in mitochondrial fusion, mitochondria–endoplasmic reticulum tethering, mitochondrial trafficking along axons, mitochondrial quality control and various types of cancer, in which *MFN2* has been indicated as a tumor suppressor gene. Discordant data on the mitochondrial altered phenotypes in patient-derived fibroblasts harboring *MFN2* mutations and in animal models have been reported. We addressed some of these issues by focusing on mitochondria behavior during autophagy and mitophagy in fibroblasts derived from a CMT2A^{MFN2} patient with an *MFN2*$^{650G>T/C217F}$ mutation in the GTPase domain. This study investigated mitochondrial dynamics, respiratory capacity and autophagy/mitophagy, to tackle the multifaceted *MFN2* contribution to CMT2A pathogenesis. We found that *MFN2* mutated fibroblasts showed impairment of mitochondrial morphology, bioenergetics capacity, and impairment of the early stages of autophagy, but not mitophagy. Unexpectedly, transcriptomic analysis of mutated fibroblasts highlighted marked differentially expressed pathways related to cell population proliferation and extracellular matrix organization. We consistently found the activation of mTORC2/AKT signaling and accelerated proliferation in the CMT2A^{MFN2} fibroblasts. In conclusion, our evidence indicates that *MFN2* mutation can positively drive cell proliferation in CMT2A^{MFN2} fibroblasts.

Introduction

Mitochondria form an ever-changing network because they can fuse, divide and move within cells (1), form vesicles (2), interact stably or transiently with other organelles (3), and can be degraded by mitophagy (4). It is widely assumed that mitochondrial fusion is essential because it allows the exchange of mitochondrial content (5–7). Mitofusin (MFN) 1 and MFN2 are closely related to dynamin family GTPases placed at the outer mitochondrial membranes where they establish homotypic and heterotypic interactions (8) initiating the connection among organelles (9). The inner mitochondrial membrane (IMM) fusion is then mediated by another GTPase activity, the optic atrophy 1 (OPA1) protein. MFN2 contains a Ras-binding and a GTPase domain, two transmembrane domains and two heptad repeat (HR) domains (9) that are important for fusion (10), and a membrane domain in which redox-mediated disulfide modifications could direct MFN2 oligomerization and mitochondrial fusion (11,12). Dysfunction of MFN2 has been associated with a variety of pathological conditions, including diabetes mellitus (13), obesity (14), atherosclerosis, hypertension (15), cancer (16,17) and two different human genetic diseases, i.e. Charcot-Marie-Tooth disease type 2A (CMT2A) harboring mono-allelic mutation with autosomal dominant inheritance, and multiple symmetric lipomatosis harboring bi-allelic mutations (18,19). CMT2A^{MFN2}, defined by its causal *MFN2* gene mutations (20), comprises ∼6% of familial CMT (∼22% of familial CMT2) (21,22) and is, depending upon nationality, the second or third most common cause of CMT (23–26). Among patients with CMT2A, the majority of *MFN2* mutations affect the amino-terminal GTPase and mid-protein coiled-coiled domains, with disease onset in the first 2 years of life and an aggressive clinical course. A few patients have mutations at the extreme MFN2 C-terminus and typically exhibit later onset (range 5–33 years old) and milder disease (27–29).

Several studies performed on CMT2A^{MFN2} patients' fibroblasts report extremely variable results, with little agreement on the existence of alterations of MFN2 protein levels (30,31), respiratory chain capacity, and oxidative phosphorylation (30–32), mitochondrial membrane potential (32) or mitochondrial DNA (mtDNA) content (30,31). Studies in transgenic mice have been equally difficult to interpret (33–35).

Received: June 10, 2022. **Revised:** August 12, 2022. **Accepted:** August 16, 2022

Although it is widely assumed that CMT2A pathogenesis largely depends on an impaired fusion between mitochondria (36) it has been observed that MFN1 can replace MFN2 as a mitochondrial fusion factor (37,38), but only *MFN2* mutations can cause disease. Interestingly, several reports support other different functions of MFN2 emerged as MFN2, but not MFN1, is also localized at the level of the mitochondria-associated endoplasmic reticulum (ER) membrane (MAM) to connect the two organelles (39,40). Notably, in a study in three CMT2A^{MFN2} patients' fibroblasts with different mutations in *MFN2*, no impairment of respiratory chain function but some alterations of ER–mitochondrial connectivity and MAM function were found and correlated with disease severity (41). Considering *MFN2* mutations in CMT2A neurons, the distal axon dies whereas the proximal part and the soma are spared implicating that mitofusins participate in mitochondrial transport, which could explain the selective die-back of long peripheral nerves in CMT2A (34,42,43). In addition to impaired fusion and transport, it must be also considered that MFN2 plays a unique role in mitophagy (44). However, impaired mitophagy is not considered a feature of CMT2A (45). Both an *in vitro* study of *MFN2*^{A383V} induced Pluripotent Stem Cells (iPSCs)-derived motor neurons (44), and an *in vivo* study of *MFN2*^{R94Q} mouse (38), suggest that mitophagy is either not changed or increased perhaps as a compensatory reaction to respiratory dysfunction in fusion-defective organelles (45). Indeed, mitochondrial dynamic proteins are profoundly involved in autophagic processes, and the role of MFN2 on autophagy/mitophagy, in cardiomyocytes (46), skeletal muscle (47) and neurons (48) has been investigated. No study deeply investigated MFN2 in cell autophagy in CMT2A patients' fibroblasts. Moreover, autophagy is often considered a mutually exclusive process with respect to cell-cycle progression (49), as many signaling pathways exhibit opposing effects on them and need to be coordinated. Both positive growth signaling and autophagy are closely linked to the energy availability in the cell, which is largely sensed through cellular levels of ATP and by the AMPK pathway (50). The PI3K-TOR pathway plays a central role in regulating growth control. Relevant to human disease is the loss of TORC inhibitors (e.g. PTEN, LKB1, TSC1/2) or constitutive activation of TORC (e.g. hyperactive PI3K or Ras signaling), which results in both sporadic cancers and cancer predisposition syndromes (51,52). Most of the studies have been performed in tumor cells where autophagy has indeed bivalent significance in response to diverse nutrient conditions, possibly acting as either a tumor-suppressive or a tumor-promoting pathway (53–56). In pancreatic cancer, MFN2 has been found to induce cell autophagy by inhibiting the PI3K/Akt/mTOR signaling pathway (57).

The present study provides the first evidence that CMT2A^{MFN2} fibroblasts harbor functionally impaired mitochondria that do not accumulate despite a defect of the initial steps of autophagy while performing an acceleration of cell division. So far, *MFN2* is considered a tumor suppressor gene in various types of cancer, to our knowledge, this is the first report of increased proliferation of CMT2A patients' fibroblasts driven by *MFN2* mutation.

Results

CMT2A^{MFN2} patient

The case presented is a severely affected 8-year-old girl who had normal early motor and language developmental milestones. She acquired autonomous ambulation at 16 months but the mother reports having noticed club foot and clumsiness in walking since then. During an orthopedic evaluation, she underwent a neurophysiological examination denoting findings compatible with a sensory-motor axonal polyneuropathy in the legs. Brain and spine magnetic resonance imaging was normal though the latter showed images compatible with a hyperintense formation (e.g. a lipoma) extended caudally from L1–L2 to S1–S2. The patient showed a stepping gait with difficulty walking on toes and heels at the examination. Whilst upper limbs were spared, she presented weakness mostly in the distal legs (MRC 3). Deep tendon reflexes in the legs were absent bilaterally. Cerebellar tests were correctly performed. Cranial nerves were normal, though the patient presented minimal visual disturbances. We obtained written informed consent for performing blood sampling, genetic tests, skin biopsy to derive fibroblast culture, and publishing reports, from her parents. The study approved by Comitato Etico Pediatrico Toscano, cod 015/2015.

Whole exome sequencing (WES) was done by precise filtering and prioritization of 476 rare (<0.01%) and pathogenic/likely pathogenic/VOUS variants in 14 rare genes with a customized in-house bioinformatics pipeline as reported in (58). Sanger sequencing of the *MFN2* gene in the CMT2A patient revealed a rare, likely *de novo* heterozygous single nucleotide substitution c.650G > T in exon 7, which changes the highly conserved cysteine at position 217 of the MFN2 protein to phenylalanine (p.Cys217Phe), located between the G3 and G4 motive of the highly conserved GTPase domain (the nomenclature of variant refers to NM_001127660.2 and NP_001121132.1). The p.Cys217Phe variant was classified as 'likely pathogenic' based on ACMG Guidelines (59), with evidence of pathogenicity PM1, PM2, PP2 and PP3. The mutation is absent from controls in Genome Aggregation Database (GnomAD) and several computational data predict a deleterious effect on the gene or gene product. This mutation was classified as *pathogenic* by MVP (https://github.com/ShenLab/missense), REVEL (https://labworm.com/tool/revel) and EIGEN (http://www.columbia.edu/~ii2135/eigen.html), as *damaging* by FATHMM-MKL (http://fathmm.biocompute.org.uk/fathmmMKL.html), DEOGEN2 (http://deogen2.mutaframe.com), DANN (https://cbcl.ics.uci.edu/public_data/DANN), SIFT (http://sift-dna.org) and PrimateAI (https://github.com/Illumina/PrimateAI), as *disease-causing* by Mutation Taster (https://www.mutationtaster.org), as *medium* by Mutation Assessor (http://mutationassessor.org/r3) and as *probably damaging* by PolyPhen2 (http://genetics.bwh.harvard.edu/pph2).

Both parents tested by Sanger sequencing on blood DNA were negative for the mutation. This mutation's genetic and clinical features have been recently described in an Asian patient affected by a severe form of CMT2A, with early disease onset (60).

Alteration of mitochondrial morphology in CMT2A^{MFN2} fibroblasts

Mitochondrial morphology in *MFN2* mutated fibroblasts can display marked changes in the mitochondrial shape suggesting MFN2 plays a direct role in maintaining mitochondrial tubular shape (38,61,62) and can range from fragmented mitochondria (63) to no alterations of mitochondrial morphology (30,32,41,64). We studied the mitochondrial morphology of CMT2A^{MFN2} fibroblasts by immunofluorescent microscopy in different experimental conditions. The cells were grown either in glucose or in galactose medium because galactose forces the cells to rely predominantly on the ATP produced by the oxidative phosphorylation (OXPHOS) system, emphasizing a possible OXPHOS defect when present. The CMT2A^{MFN2} were different from the control-fibroblasts both regarding the shape ratio, expressed as a percentage of tubular, intermediate and fragmented mitochondria, and regarding the efficiency in restoring the basal network either in glucose- or in galactose-medium (Fig. 1A). CMT2A^{MFN2} fibroblasts showed

that the percentage of intermediate mitochondria population in the basal condition was significantly higher to control cells when grown in glucose-medium (Fig. 1A). We then exposed the fibroblasts to the uncoupling agent carbonyl cyanide m-chlorophenyl hydrazine (CCCP), a proton ionophore that collapses the proton electrochemical gradient across membranes, to investigate the capacity of these cells to recover a normal mitochondrial network (Fig. 1A; *CCCP + Re*). Upon CCCP treatment, we appreciated a decrease in the intermediate mitochondria population and a striking increase in the fragmented ones in CMT2A^{MFN2} compared to control fibroblasts indicating a lower capacity of the mitochondrial network remodeling in the mutated cells (Fig. 1A). The fragmented mitochondria population was reduced in CMT2A^{MFN2} when CCCP was removed although the recovery did not return to the pre-CCCP level, especially in glucose-medium (Fig. 1A). When we analyzed the mitochondrial network in fibroblasts grown in galactose-medium, we observed that the mitochondrial network's fragmentation and the failure in rescuing the network morphology were exacerbated (Fig. 1A).

CMT2A ^{MFN2} fibroblasts show normal MFN2 and OPA1 and increased DNM1L/DRP1 protein levels

We explored the possibility that the altered mitochondrial network morphology was due to *MFN2* haploinsufficiency and diminished MFN2 protein levels. We quantified the steady-state levels of MFN2 protein in CMT2A^{MFN2} and control total homogenates by western blot. The total amount of MFN2 protein was not significantly changed in basal conditions in CMT2A^{MFN2} compared to control. When both mutant and control fibroblasts were treated with CCCP, the MFN2 protein level was not significantly changed (Fig. 1B). To study other main protein components involved in the machinery of mitochondrial fusion/fission, we measured optic atrophy 1 (OPA1) and DNM1L/DRP1 (dynamin-related protein 1) levels by western blot analysis (Fig. 1B). OPA1 is a key mitochondrial dynamics protein, localized in the inner membrane where it controls cristae structure (65). There are eight alternatively spliced *OPA1* isoforms, that include a long l-OPA1 and short s-OPA1 (66) isoforms cleaved by the IMM peptidase OMA1 that responds to mitochondrial membrane potential dissipation, which is essential in maintaining mitochondrial morphology (66,67). The DNM1L orchestrates mitochondrial fission after translocation from the cytosol to mitochondria (68). Alteration of the ratio between MFN2 and DNM1L has been found as responsible for initiating mitophagy (69). We found that the total amount of OPA1, as well as the l-OPA1:s-OPA1 ratio, was unchanged between mutant and control fibroblasts both in basal condition and following CCCP treatment (Fig. 1B).

Conversely, in basal conditions, we found an enhanced DNM1L protein expression in CMT2A^{MFN2} compared to control fibroblasts; particularly, the expression was almost undetectable in control fibroblasts. Furthermore, a marked increase in DNM1L protein expression following CCCP mitochondria depolarization was found compared to the steady state in both mutant and control cells (Fig. 1B). Mitochondrial fragmentation observed in CMT2A^{MFN2} fibroblasts could be mediated by the increased DNM1L expression found in the steady state and as previously reported, these can be considered early and key events observed in a wide range of neurodegenerative disorders (70). Transcriptomic analysis showed unaltered levels of all the mitochondrial dynamics proteins in CMT2A^{MFN2} fibroblasts (MFN2 GFOLD ≤ -0.0338323; OMA1 GFOLD = 0; DNM1L GFOLD = −0.115974; Supplementary Material, Table S1).

Alteration of membrane potential and reduced bioenergetics capacity in CMT2A^{MFN2} fibroblasts

Considering that mitochondrial fragmentation is often associated with mitochondrial depolarization (71), we then assessed the mitochondrial membrane potential ($\Delta\psi M$) by JC-1 staining of cultured fibroblasts that promotes the formation of red fluorescent JC-1 aggregates in cells with high potential, while a diffuse green fluorescence in the cells with low membrane potential. CMT2A^{MFN2} fibroblasts showed red fluorescence decay and a correspondent decrease of the red/green intensity ratio with respect to the control fibroblasts (Fig. 2A). MFN2 has been shown to play a key role in activating mitochondrial oxidative metabolism (72–74). We, therefore, asked if mutations in CMT2A^{MFN2} fibroblasts affected bioenergetics. We measured the oxygen consumption rate (OCR) in control and patient-derived intact cells using an oxygen electrode to measure the OCR in intact cells (Fig. 2B). We measured the endogenous respiration rate as basal respiration and after adding a proton ionophore (2,4-dinitrophenol) to uncouple respiration. There was a significant decrease (43%) in the baseline respiration in MFN2$^{650G>T}$ fibroblasts compared to control cells (Fig. 2B). Polarographic assays estimated a reduction of 65.4% for Complex I, 50.7% for Complex II + III and 35% for Complex IV activities in CMT2A^{MFN2}cells compared to control cells (Fig. 2B). These findings showed that the monoallelic missense *MFN2* mutant fibroblasts involved significant alteration of the respiratory complexes' activities. To further explore whether the reduced oxygen consumption was due to altered mitochondrial biogenesis and/or integrity of the mitochondrial genome we assessed mtDNA *status*. We found intact, full-length genomic mtDNA (Fig. 2C) and no major rearrangements, although cell cultures are not appropriate to identify major deletions of mtDNA. The mtDNA/nDNA (mitochondrial to nuclear DNA ratio) levels were not statistically significantly changed in CMT2A^{MFN2} compared to the control fibroblasts (Fig. 2D). The overlay of transcriptomic data to the KEGG (Kyoto Encyclopedia of Genes and Genomes) oxidative phosphorylation pathway shows an unaltered expression of genes encoding for mitochondrial respiratory chain complex enzymes, except for ATP6V0E2 (GFOLD = −1.533) which was found to be slightly downregulated in CMT2A^{MFN2} cells (Supplementary Material, Fig. S1).

CMT2A^{MFN2} fibroblasts exhibit impaired autophagy

To assess if the mutant form of MFN2 may affect the autophagy process, we analyzed the microtubule-associated protein 1 light chain 3 (MAP1LC3/LC3) and SQSTM1/p62 (sequestosome 1) levels, two known markers of autophagy and autophagy-related structures. During autophagy, LC3B-II, a lipidated form of LC3B-I, serves as a marker of successful autophagosome formation since it is a major component of the autophagosome membrane (75). SQSTM1, a prominent autophagy receptor family member, binds ubiquitinated macromolecules and forms the core of the autophagosomal cargo routed for degradation (76). The expression of LC3B-II itself does not reflect the downstream process of autophagy, indicated as autophagy flux (77). It has to be considered also the expression of SQSTM1, which increases during the molecular accumulation process and decreases as the enzymatic hydrolysis reactions start. Therefore, the decrease of SQSTM1 expression and the transformation of LC3B into LC3B-II are important indicators of autophagy flux.

CMT2A^{MFN2} and control fibroblasts were analyzed by western blot to assess the levels of autophagy under basal conditions.

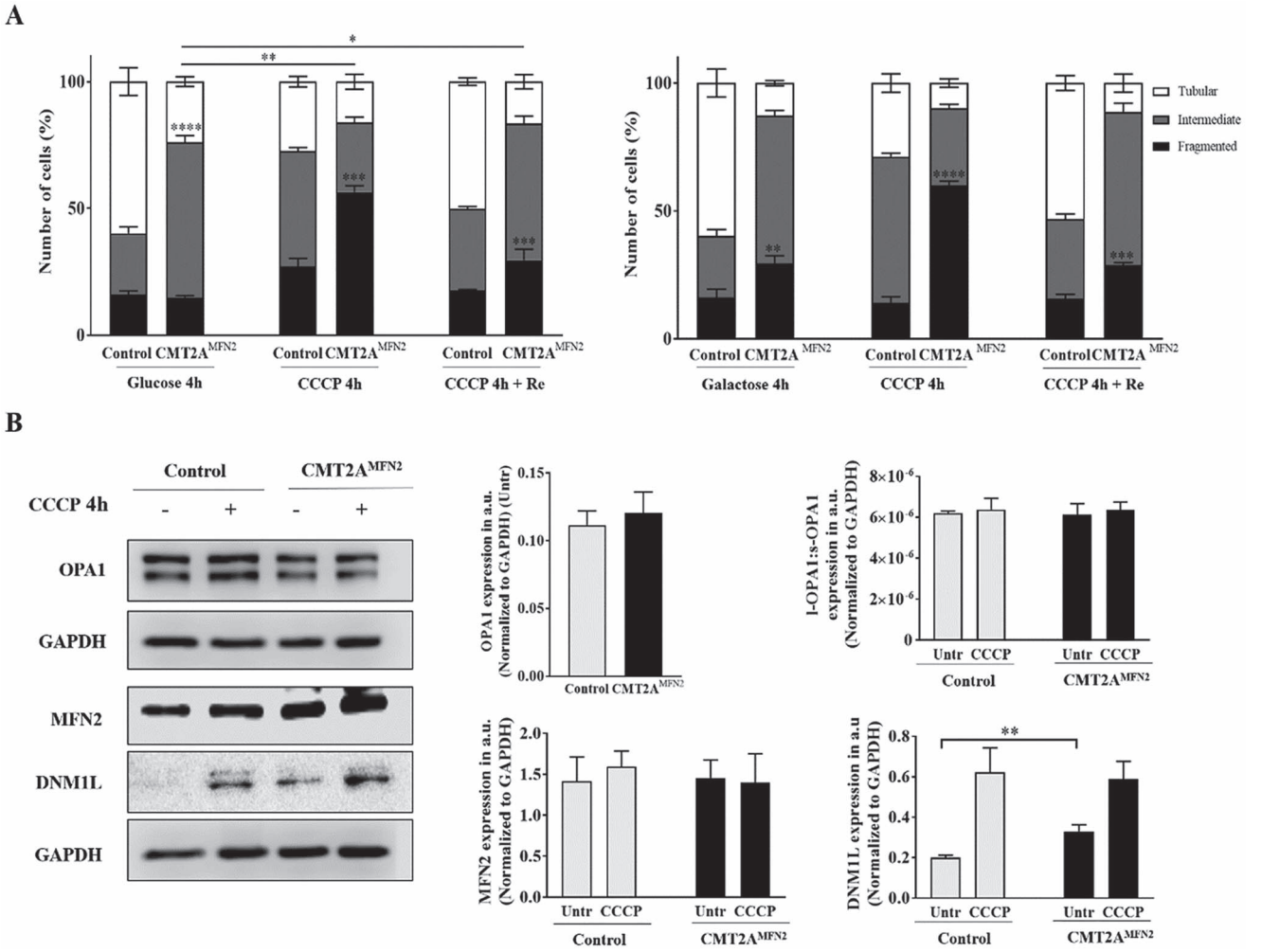

Figure 1. Mitochondrial network morphology is impaired and the pro-fission DNML1 but not the pro-fusion proteins are increased in CMT2A^{MFN2} fibroblasts. (**A**) Bar graphs show fibroblasts distribution incubated in either DMEM-glucose or DMEM-galactose medium, into three different categories based on mitochondrial morphology: tubular, intermediate and fragmented mitochondrial. Immunolabeling of mitochondria shows fragmentation in CMT2A ^{MFN2} fibroblasts. Primary fibroblast cultures were treated for 4 h with 10 μM of CCCP (CCCP) and treated with CCCP followed by 4 h in the initial medium (CCCP + Re). The mitochondrial network was visualized by a VDAC-1 antibody and DAPI staining was used to visualize cell nuclei. Data are presented as mean ± SD of three independent experiments ($n = 3$). Student's t-test; *$P < 0.05$; **$P < 0.01$; ***$P < 0.001$ and ****$P < 0.0001$. One-way ANOVA test with Bonferroni's correction was performed to compare the mean of fragmented mitochondria following CCCP induction or CCCP and Re to the mean of fragmented mitochondria in the base condition in CMT2A ^{MFN2} fibroblasts. (**B**) Representative western blot image of OPA1, MFN2 and DNM1L in total lysates from control and patient-derived cells in basal conditions and after treatment for 4 h with 10 μM of CCCP. Each band was normalized to GAPDH band density and a densitometrical analysis was performed. Densitometrical analysis shows total OPA1 (l-OPA1 + s-OPA1) level in untreated (Untr) condition; ratios of the l-OPA1 to the s-OPA1 isoforms, MFN2 and DNIM1L levels for each condition. Data are presented as mean ± SD ($n = 3$). Student's t-test; *$P < 0.05$; **$P < 0.01$ and ***$P < 0.001$.

CMT2A^{MFN2} showed decreased LC3B-II levels and accumulation of SQSTM1 compared to control fibroblasts (Fig. 3). These results indicated a lower number of autophagosomes and a low autophagic response. We then assessed the consequences of autophagy induction by Torin1, an ATP-competitive inhibitor of the mechanistic target of rapamycin kinase complex (mTORC). Upon induction of autophagy, CMT2A^{MFN2} fibroblasts displayed higher LC3B-II levels compared to the basal conditions as well as it is shown in control fibroblasts (Fig. 3), demonstrating that the autophagic machinery was functional. However, when we compared the LC3B-II levels between the CMT2A^{MFN2} and control fibroblasts in the same conditions as above, we found about a 20% decrease, meaning that in mutant cells there is a lower formation of autophagosomes (Fig. 3). We then analyzed CMT2A^{MFN2} fibroblasts by treating the cells with chloroquine (CQ), a lysosomotropic agent that inhibits either autophagosome fusions with lysosome or lysosomal protein degradation, thereby blocking the degradation of LC3B-II. This inhibition halts the autophagic machinery and allows assessment of the induction of intrinsic autophagy in cells. We found that upon CQ treatment, CMT2A^{MFN2} fibroblasts showed reduced accumulation of LC3B-II (Fig. 3). These results mirrored the data obtained in basal and Torin1 conditions, suggesting that the autophagy induction is overall reduced in CMT2A^{MFN2} fibroblasts.

Assessment of mitophagy in the CMT2A^{MFN2} fibroblasts

Next, the elimination of mitochondria through CCCP-induced mitophagy was evaluated on fibroblasts with immunofluorescence staining with LC3B and TOMM20 (translocase of outer mitochondrial membrane 20) antibodies. Despite the few autophagosomes, a larger number of them were engaged in engulfing

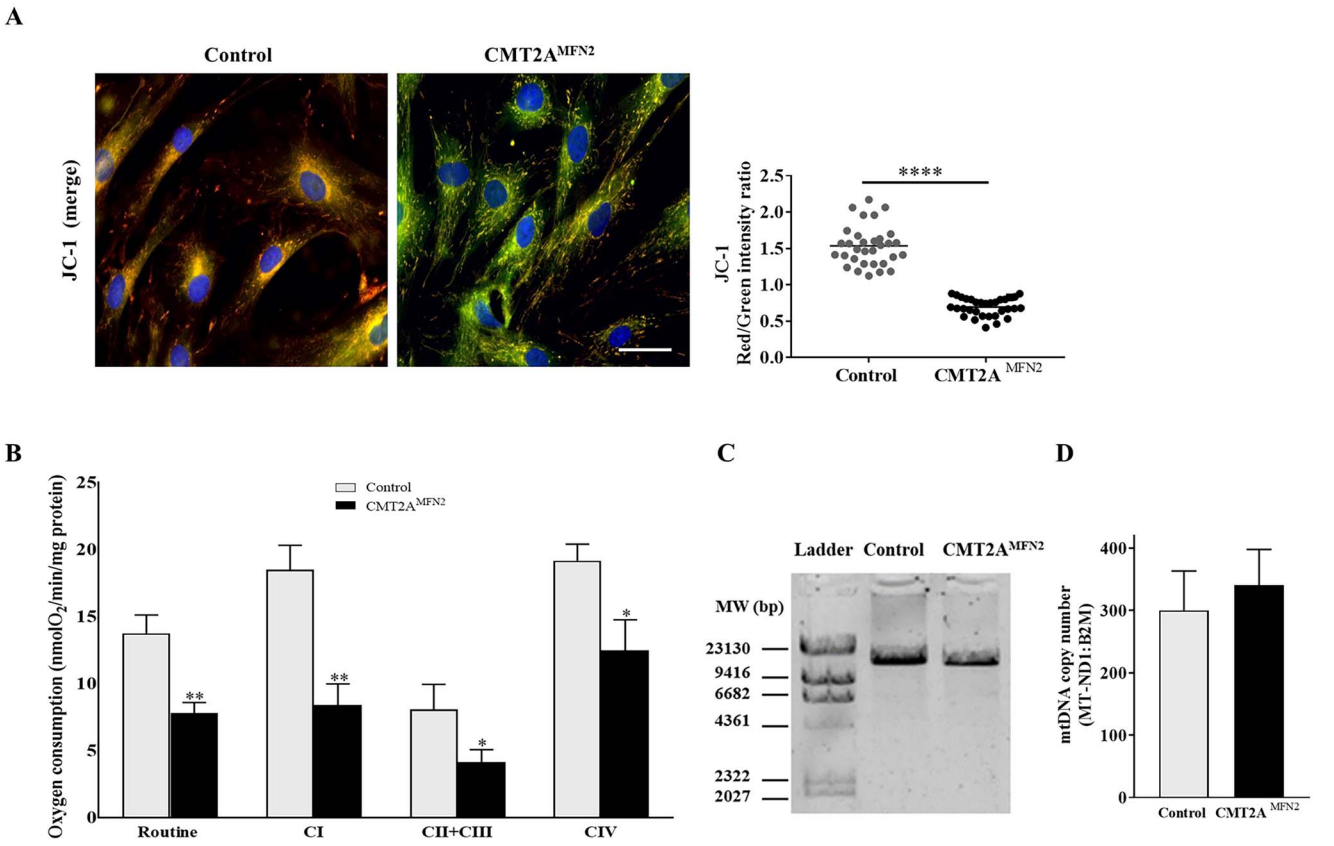

Figure 2. Mitochondrial membrane potential and bioenergetics capacity are altered whereas mitochondrial DNA integrity and steady-state levels are unchanged in CMT2A^{MFN2} fibroblasts. (**A**) The mitochondrial membrane potential ($\Delta\Psi$m) was measured in control and CMT2A ^{MFN2} via the JC-1 staining. Red fluorescence is an index of $\Delta\Psi$m preservation, whereas green fluorescence is an index of mitochondrial membrane depolarization. Scale bars equal to 25 μm. The individual value plot displays the red/green intensity ratio. (**B**) Measurement of endogenous respiration rates in digitonin-permeabilized cells was performed to compare OCRs of control and CMT2A^{MFN2} fibroblasts measured under basal (routine respiration) and substrate-driven respiration conditions, as described in Materials and Methods. Bars represent the mean respiration rate expressed as nmoles O_2/min/mg protein. Data are presented as mean ± SD of three independent experiments ($n = 3$). CI: Complex I; CII: Complex II; CIII: Complex III; CIV: Complex IV. (**C**) Evaluation of mtDNA integrity performed by long-range PCR resulted in a 16.5 kb PCR fragment representing the full size of the mitochondrial genome in both control and CMT2A^{MFN2} fibroblasts, as visualized on 0.8% agarose gel. (**D**) Quantification of mtDNA copy number in CMT2A^{MFN2}and control fibroblasts. qRT-PCR analysis of mtDNA measures the mtDNA copy number expressed as mtDNA:nDNA indicative of the relative number of mtDNA per cell. For more details, see Materials and Methods. Data are presented as mean ± SD of three independent experiments ($n = 3$). Student's t-test; $^*P < 0.05$; $^{**}P < 0.01$ and $^{***}P < 0.001$.

mitochondria in CMT2A^{MFN2} compared to control fibroblasts, as shown by measuring LC3B/TOMM20 colocalization (LTc): TOMM20 (T) dots/cell. Furthermore, the LTc: T dots/cell in CMT2A^{MFN2} fibroblasts did not significantly change regardless of the treatment conditions (Fig. 4A). To gain further insight into the autolysosome formation in stressful conditions for mitochondria, we extended our studies by performing immunolabeling with LC3B and LAMP1 (lysosomal associated membrane protein 1) during CCCP treatment (Fig. 4B). The ratio of the number of LC3B/LAMP1 (LLpc): LAMP1 (Lp) dots/cell, representing the portion of lysosomes fusing with autophagosomes, was significantly increased (9-fold) in CMT2A^{MFN2} fibroblasts already in basal conditions (Fig. 4B). The LLpc: Lp dots/cell in CMT2A^{MFN2} fibroblasts did not change regardless of the treatment conditions (Fig. 4B). Overall, these results indicate that when mitophagy is stimulated, the formation of mitophagosomes and autolysosomes in CMT2A^{MFN2} occurs as in the control fibroblasts.

When we examined the expression of both LC3B and parkin RBR E3 ubiquitin-protein ligase (PRKN), we found that LC3B/PRKN colocalization (LPrc) was already increased in untreated CMT2A^{MFN2} compared to control cells (Supplementary Material, Fig. S2A and D). Then, we investigated if the proteins implicated in the mitochondrial recycling process, PTEN-induced kinase 1 (PINK1) and PRKN, were deregulated or mislocalized in mutated CMT2A^{MFN2} fibroblasts. Confocal microscopy on CMT2A^{MFN2} fibroblasts showed a non-significant change in PINK1 (Supplementary Material, Fig. S2B, C and E), whereas a significant increase in PRKN levels compared with the control sample was found after 4 h of treatment with CCCP (Supplementary Material, Fig. S2A, C and G). We determined the number of PINK1-recruited mitochondria as PINK1/TOMM20 colocalization (PTc): PINK1 (P) dots/cell (Supplementary Material, Fig. S2B and F) and PINK1/PRKN colocalization (PPrc) dots/cell that was increased in untreated CMT2A^{MFN2} compared to control cells and did not change upon CCCP treatment (Supplementary Material, Fig. S2C and H). Overall, these results indicate that mitophagy is already activated in CMT2A^{MFN2} fibroblasts.

Transcriptome profiles of CMT2A ^{MFN2} fibroblasts

To evaluate perturbed gene expression in mutated CMT2A^{MFN2} fibroblasts we performed RNA-seq analysis *versus* normal control fibroblasts. Raw data are freely available at the SRA database upon the BioProject accession number PRJNA868927. In the patient CMT2A^{MFN2,} we identified 1229 Differentially Expressed Genes (DEG) of which 763 were under-expressed and 466 were over-expressed, with an adjusted fold change (GFOLD)

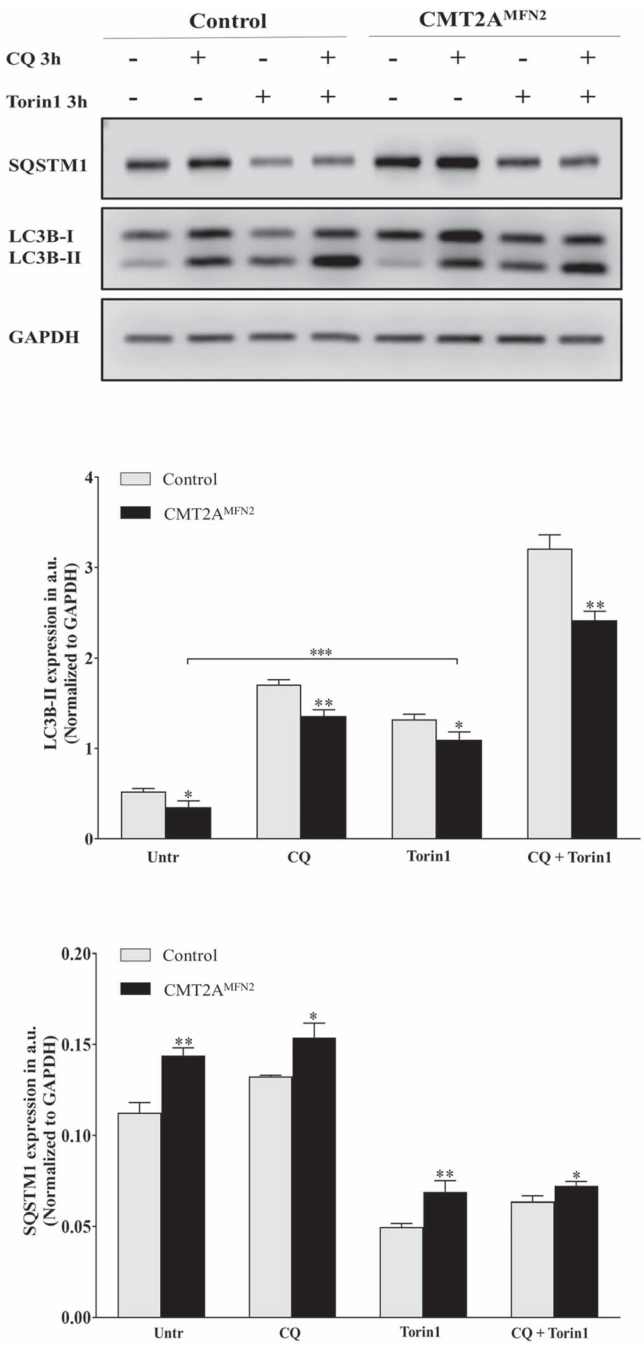

Figure 3. Autophagosome synthesis is reduced in CMT2A^{MFN2} fibroblasts. Representative western blot for the investigation of autophagy-related protein expression in CMT2A^{MFN2} fibroblasts. Fibroblast cells were incubated under normal conditions or treated with 50 μM CQ for 3 h in the absence or presence of 1 μM of Torin1. Western blotting was performed for LC3B and SQSTM1 in total cell lysates from control and patient-derived cells for each condition. Each band was normalized to GAPDH band density and densitometrical analysis of LC3B-II and SQSTM1 levels for each condition was performed. Data are presented as mean ± SD, $n = 3$. Student's *t*-test; *$P < 0.05$; **$P < 0.01$ and ***$P < 0.001$.

value equal to or greater than 1.5 in absolute value and a *P*-value < 0.05. To investigate the function of the DEGs, gene ontology (GO) term enrichment analysis was conducted with the online software Database for Annotation, Visualization, and Integrated Discovery database (DAVID). In general, the DEGs were significantly enriched in the following biological processes (BPs), molecular functions (MFs) and cellular components (CCs, Supplementary Material, Table S2). In the BPs group, DEG was mainly enriched in *cell adhesion* ($N = 73$,1.30E-11), *extracellular matrix organization* ($N = 33$, 3.90E-09), and processes in line with the maintenance of structural integrity, the primary function of fibroblasts. The third most enriched BP is the *positive regulation of cell proliferation* ($N = 56$, 5.60E-05), revealing 56 DEGs: 19 up-regulated and 37 down-regulated genes. In the CCs group, aberrantly expressed genes localized in the extracellular region ($N = 196$, 1.30E-18) or were integral components of the plasma membrane ($N = 140$, 6.50E-14) or belonged to the extracellular matrix molecules ($N = 48$, 1.20E-13). In the MFs group, most of the DEGs were extracellular matrix structural constituents ($N = 33$, 1.10E-10), extracellular matrix structural constituents conferring tensile strength ($N = 14$, 2.20E-05), and integrin, and heparin-binding molecules. According to the KEGG pathway enrichment analysis, the DEGs were enriched in protein digestion and absorption ($N = 21$, 1.70E-04), axon guidance ($N = 28$, 2.60E-04), amoebiasis and PtdIns3K -AKT signaling pathway (1.40E-03).

The protein–protein interaction (PPI) network analysis was constructed with STRING, which integrates both known and predicted PPIs and can be applied to predict functional interactions of proteins (78,79). A network was generated containing 1514 nodes and 968 interactions with a minimum required interaction score > 0.8 and only query proteins were displayed (Supplementary Material, Fig. S3). The most significant six sub-modules of the network (MCODE score > 5) have been evidenced with pink circles (Supplementary Material, Fig. S3; Table S3). The BiNGO analysis showed that the first sub-module was enriched with statistically significant GO Biological Processes mostly involved in the mitotic cell cycle, microtubule-based processes, microtubule cytoskeleton organization, cell cycle phases, chromosome segregation, mitosis, M phase of the mitotic cell cycle were all found to be down-regulated (Supplementary Material, Fig. S3; Table S3). The second cluster involved processes relating to cell–substrate adhesion and cell–matrix adhesion while the third cluster involved processes relating to the extracellular matrix organization. The most significant KEGG pathways associated with the PPI network were Axon guidance ($P = 1.30E-12$), Focal adhesion ($P = 7.51E-12$) and again the PtdIns3K-AKT signaling pathway ($P = 2.07E-11$). Insulin-like growth factor 1 (IGF1) is the most up-regulated gene of the *PtdIns3K-AKT signaling pathway* (3.73-fold change) (Supplementary Material, Fig. S3).

As far as the genes correlated with autophagy (80), we found RAB39B, DEPTOR, EIF4EBP1, MAP1LC3C and SESN2 among the up-regulated autophagy genes; PI3K3R3, E2F1, RAB37, amongst the down-regulated ones (Supplementary Material, Fig. S4). Of the first group, two overexpressed genes encode proteins that negatively regulate mTORC1, i.e. DEPTOR (DEP domain with mTOR interacting protein) and SESN2 (Sestrin 2); EIF4EBP1 represents a downstream mTORC1 effector; as well as MAP1LC3C, an important LC3B paralog. Two RAB (Ras analog in the brain) proteins, the overexpressed RAB39B and the sub-expressed RAB37 are important in the formation of autophagosomes (81–83).

These RNA-seq data were also used to evaluate the presence of the mutant mRNA with respect to the wild-type to infer some clues on the possibility that the mutant form of the protein was expressed. We checked the reads coming from the position of the mutation of the mRNA at residue p.Cys217Phe. The findings in CMT2A^{MFN2} fibroblasts support the presence of the variant in MFN2 mRNA, in fact, on 114 total reads, 49 support the mutated

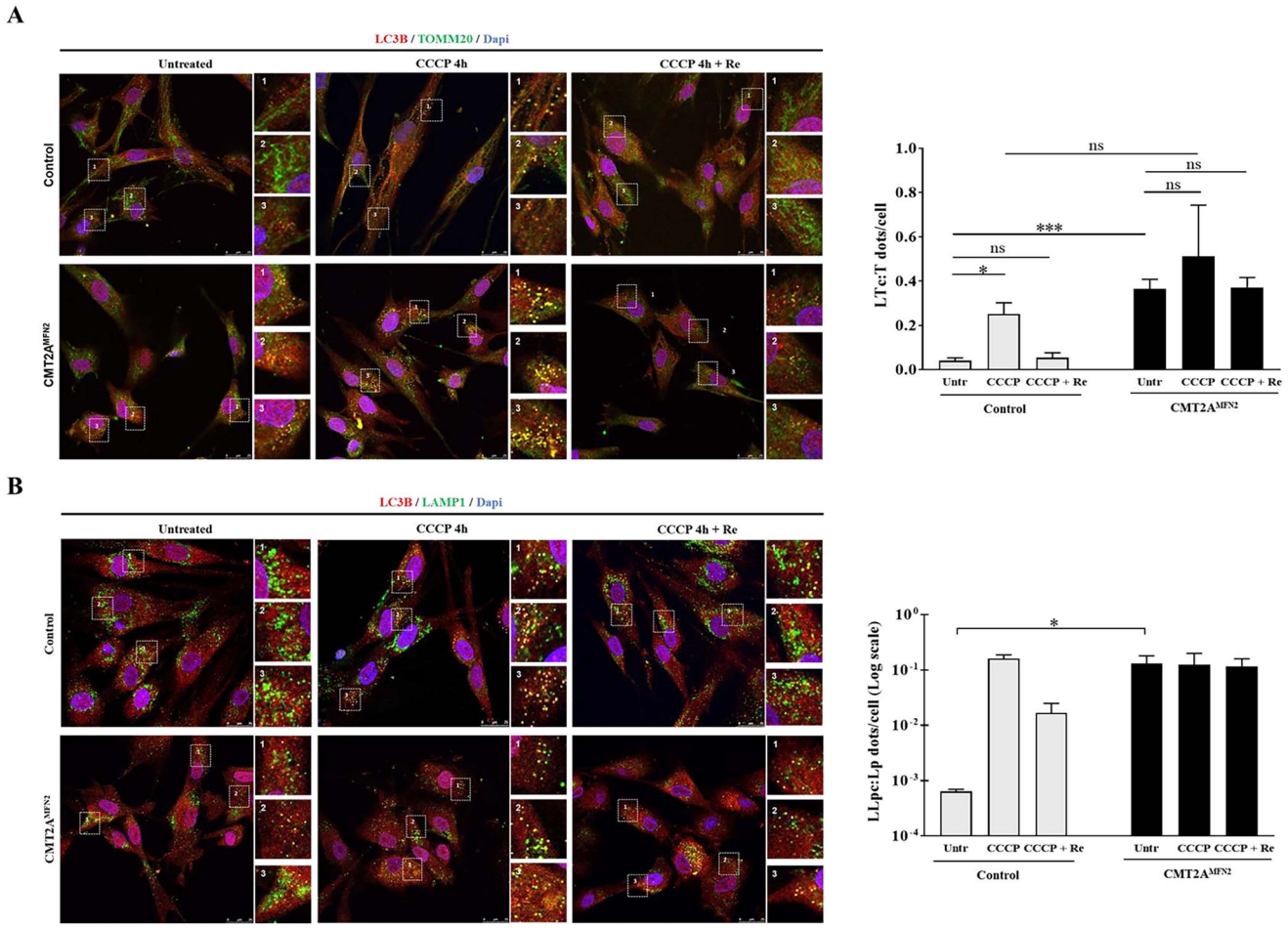

Figure 4. The formation of mitophagosomes and autolysosomes is not impaired in CMT2A^{MFN2} cells. Fibroblasts were incubated under normal conditions (untreated), treated for 4 h with 10 μM of CCCP (CCCP 4 h) and treated with CCCP followed by 4 h in the initial medium (CCCP 4 h + Re). (**A**) Cells were fixed and labeled with anti-LC3B (red) and anti-TOMM20 (green) and counterstained with DAPI (blue) for each condition. Quantification of the ratio between LC3B and TOMM20 colocalization (LTc, in yellow) and TOMM20 (T) expressed as LTc: T dots/cell. (**B**) Cells were fixed and labeled with anti-LC3B (red) and anti-LAMP1 (green) and counterstained with DAPI (blue) for each condition. Quantification of the ratio between LC3B and LAMP1 colocalization (LLpc, in yellow) and LAMP1 (Lp) expressed as LLpc: Lp dots/cell. Scale bars equal to 25 μm. Values are expressed as mean ± S.D. ($n = 3$ independent experiments). Student's *t*-test; *$P < 0.05$; **$P < 0.01$ and ***$P < 0.001$. One-way ANOVA test with Bonferroni's correction was performed for multiple comparisons.

variant T (43%) and 65 reads support the wild-type nucleotide (57%). Accordingly, Sanger sequencing with the reverse primer of the PCR amplified cDNA region including the mutation, showed that the mutant allele is present at a slightly lower level with respect to the wild-type one (Supplementary Material, Fig. S5). The control fibroblasts lacked the mutation at that nucleotide position.

CMT2A ^{MFN2} fibroblasts showed consistently higher growth rates than control fibroblasts

Since transcriptomic data highlighted strong changes in the expression of genes/pathways associated with cell proliferation including the class I phosphatidylinositol 3-kinase (PtdIns3K) pathway (84), we performed the growth curve of CMT2A ^{MFN2} and control fibroblasts in glucose medium. We observed an immediate and intensive log phase until the third day of CMT2A ^{MFN2} fibroblasts. The CMT2A^{MFN2} fibroblasts' curve showed that the final plateau started on the third day, while in control cells it started on the fourth day. An increased number of CMT2A ^{MFN2} cells were present from day 1 to 3 post-seeding as compared to control cells. The doubling time was reduced by 59% in CMT2A ^{MFN2} fibroblasts compared to control (Fig. 5A).

The serine/threonine-protein kinase AKT is increasingly phosphorylated at Ser473 in CMT2A^{MFN2} fibroblasts

The transcriptomic data led us to hypothesize the involvement of the PtdIns3K pathway, known to promote cell proliferation, in the increased cell proliferation rate of CMT2A^{MFN2} fibroblasts. Particularly, we found an up-regulation of IRS2 (insulin receptor substrate 2) and IGF1, two known upstream regulatory elements of the PtdIns3K/AKT pathway. Since the serine/threonine-protein kinase AKT is a major signal transducer of the PtdIns3K pathway in all cells and tissues, we investigated AKT activation. After the activation of PtdIns3K and subsequent recruitment of AKT to the plasma membrane (85), AKT is partially activated through initial phosphorylation at Thr308 by phosphoinositide-dependent kinase-1 (PDK1) and then fully activated by the phosphorylation at Ser473 by mTORC2 (86–90). The full activity of AKT depends on its total protein concentration and on the phosphorylation level of both the Thr308 and Ser473 residues which report on

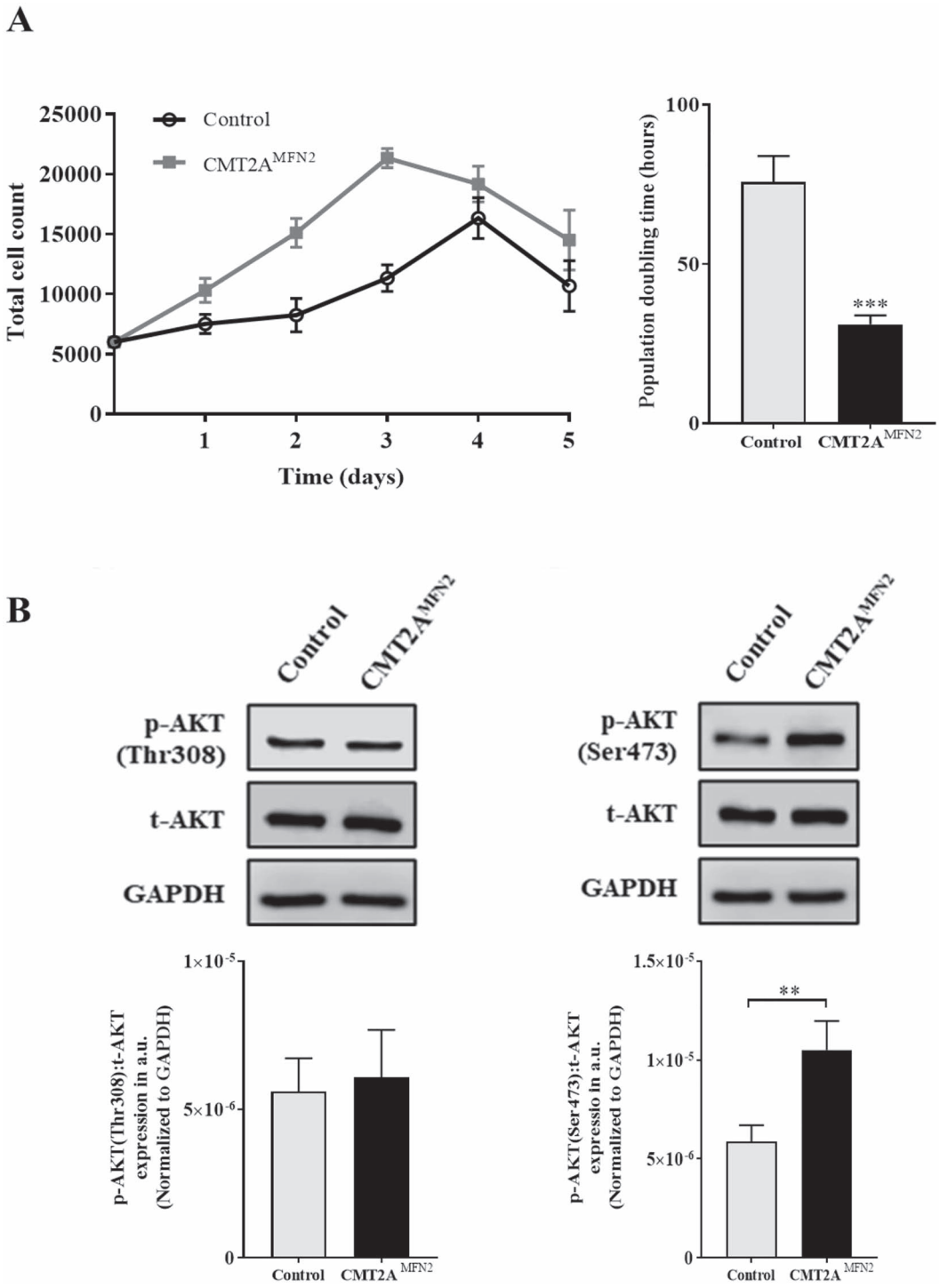

Figure 5. CMT2A^{MFN2} fibroblasts exhibit a high growth rate associated with increased phosphorylation of AKT-Ser(473), but not Thr(308), in CMT2A^{MFN2} fibroblasts. (**A**) Growth curves and population doubling time for CMT2A ^{MFN2} and control fibroblasts grown in 24-well plates over 5 days. 6000 cells were seeded in 10% FBS serum supplemented with complete DMEM culture media. Doubling time was calculated from day 0 to day 1 by cell counting method and using the following formula: PD = t x Log2/(LogC2 – LogC1). [PD = Population doubling time, t = 24 h (interval of cell count), Log = 10 based Log, C1 = 1st cell count, C2 = 2nd cell count]. (**B**) Representative western blot images of p-AKT and t-AKT in total cell lysates from control and patient-derived cells in basal conditions. Each band was normalized to GAPDH band density and densitometrical analysis of p-AKT: t-AKT was performed. Data are presented as mean ± SD ($n = 3$). Student's *t*-test; *$P < 0.05$; **$P < 0.01$ and ***$P < 0.001$.

the upstream kinase(s) activity. Our results showed that mutant fibroblasts displayed similar total AKT steady-state levels and AKT(Thr308) phosphorylation whereas the AKT(Ser473) phosphorylation was strongly increased compared to control cells (Fig. 5B). No change in AKT(Thr308) phosphorylation suggests a normal activity of PDK1 while an increase in AKT(Ser473) phosphorylation suggests an increase in the mTORC2 activity in CMT2A^{MFN2} fibroblasts.

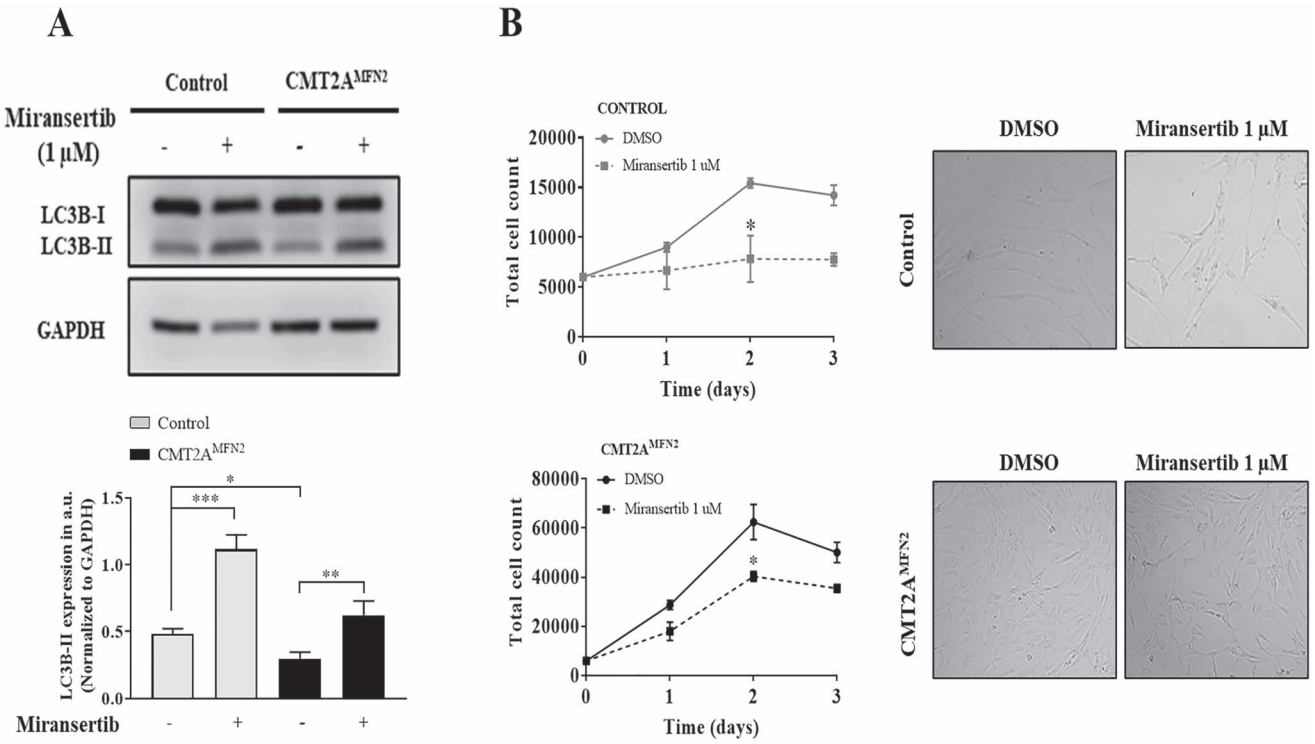

Figure 6. Pharmacological AKT inhibition restores autophagy and reduces CMT2A^{MFN2} fibroblasts' growth rate. (**A**) Representative western blot images of LC3B-II in total cell lysates from control and patient-derived cells treated both with vehicle (DMSO) and Miransertib 1 μM for 72 h. Each band was normalized to GAPDH band density and densitometrical analysis of LC3B-II was performed. (**B**) Cell growth rate of control and CMT2A^{MFN2} fibroblasts treated both with vehicle (DMSO) and Miransertib 1 μM. Representative images of cells treated both with vehicle (DMSO) and Miransertib 1 μM are shown. Data are presented as mean ± SD ($n = 3$). Student's *t*-test; *$P < 0.05$; **$P < 0.01$ and ***$P < 0.001$. One-way ANOVA test with Bonferroni's correction was performed for multiple comparisons.

Pharmacological AKT inhibition restores autophagy and reduces CMT2A^{MFN2} fibroblasts' growth rate

To prove that AKT is involved in the downregulation of the autophagy initiation and the increase of cell proliferation rate of CMT2A^{MFN2} fibroblasts, we used Miransertib, a potent and selective allosteric AKT inhibitor. We evaluated the effect of Miransertib treatment on LC3-II levels which resulted in an increase in CMT2A^{MFN2} fibroblasts compared to DMSO-treated cells (Fig. 6A). Next, we showed that the treatment caused a decrease in cellular growth rates of CMT2A^{MFN2} fibroblasts compared to DMSO-treated cells as well as of control fibroblasts (Fig. 6B). Taken together, all these data, demonstrated the dependence of both autophagy and cell proliferation on the AKT pathway.

Discussion

Although the genetic cause of CMT2A is, by definition, mutations in *MFN2* (20,21), the functional consequences linking MFN2 dysfunction to the cellular pathology underlying the neuronal die-back and neuromuscular degeneration remain not completely clarified (91). The mechanisms that have been proposed for CMT2A^{MFN} pathogenesis, besides the impairment of mitochondrial fusion and loss of fusion-related homeostatic repair (92,93) have included the rupture of mitochondria-RE connectivity that affects calcium crosstalk and phospholipid/cholesterol synthesis (41), the interruption of mitochondrial trafficking along with axons (34,93,94) and the dysregulation of mitochondrial quality control with mitochondria emptying or preservation of cytotoxic senescent and damaged mitochondria (44,91). We used fibroblasts as a model system although by now several findings have been reported in a more suitable cell system, such as neuronal-derived cells with (95) and without (44) genetic modification, but which still leaves open several questions on the contribution of *MFN2* to diseases. To gain deeper insight into the pathogenesis of *MFN2* mutations, we focused on the mitochondrial respiratory capacity, morphology and mitochondria behavior during autophagy and mitophagy in fibroblasts derived from a CMT2A patient with an *MFN2*$^{650G > T/p.\ C217F}$mutation in the GTPase domain. We obtained interesting clues on the molecular mechanisms of autophagy in CMT2A fibroblasts that, to the best of our knowledge, have not ever been reported. In our report, we found that despite the normal level of *MFN2* expression (we cannot discriminate how much of either wild-type or mutant protein form coexist in the cell), as well as the OPA1 protein in CMT2A^{MFN2} fibroblasts, mitochondria were unable to form a complete network: the population of the so-called intermediate-fragmented mitochondria was significantly high and had an inefficient capacity to recover upon removal of stressful insult. In addition, CMT2A^{MFN2} fibroblasts mitochondria resulted highly depolarized and showed impaired respiration with significant reduction of Complex I, Complex II + III and Complex IV activities, highlighting the key role of mitochondrial dynamics in maintaining mitochondrial function (74,96). These findings differ from studies in *Mfn2* gene knockout mouse embryonic fibroblast (MEF) cells, in which only CI + III and CII + III defects originated from an impaired coenzyme Q10 biosynthesis (97,98), and in MN-derived cells, in which mild multi-complex respiratory chain defect mostly impacted on

Complex II and Complex II + III activities but not Complex I (44). Intriguingly, the same fibroblast cell lines harboring the mutation out of the GTPase domain as the MN-derived cells presented alterations in mitochondrial distribution and a combined defect in the respiratory chain activity without any difference in total mitochondrial content (44). Previous findings that examined mitochondrial function in fibroblasts carrying *MFN2* mutations in the GTPase domain and with normal *MFN2* expression, reported normal respiratory complex activities, mtDNA content and mitochondrial morphology resembling the observations that those cells expressed sufficient levels of MFN1 to compensate for MFN2 defect (30,32). We also observed that the mtDNA copy number was not reduced nor did mtDNA show rearrangements, probably suggesting that defects of OXPHOS complexes are not due to impaired mtDNA transcription or translation (63). Reduced OXPHOS was not reflected in the RNA-seq analysis, suggesting that probably the functional changes herein described can be due to alteration of the mitochondrial morphology and dynamics more than to the OXPHOS expression levels. The variability of phenotypes seen by us, and the different groups (in patient cells and mice) is puzzling. We noticed that when the MFN2 mutation affects the mitochondrial dynamics also the OXPHOS system is impaired suggesting a direct correlation between the mitochondrial conformation and the respiratory complexes' functionality (74). We can add that the presence of mutant mRNA that we did find in CMT2A^{MFN2} fibroblasts likely leads to the production of a defective MFN2 protein that may have a dominant negative effect due to an inefficacy to form mitofusins homodimers and heterodimers that cause the alteration of the fusion process.

To assess whether the damaged mitochondria are properly eliminated we investigated the effect of *MFN2* mutation on cellular and mitochondrial quality control systems, namely autophagy and mitophagy (99,100). Autophagy has been implicated in the maintenance of neuronal functions and alterations in autophagy have been associated with a variety of neurodegenerative disorders (101,102) and the reports on the role of *MFN2* in autophagy/mitophagy are quite controversial (38,44,45). We evaluated the ability to discharge the defective mitochondria by autophagy/mitophagy processes. Our investigations on CMT2A^{MFN2} fibroblasts showed a reduction of the autophagosome synthesis, as suggested by the accumulation of LC3B-I and the reduced conversion to LC3B-II. On the other hand, the accumulation of SQSTM1 suggested an abnormal clearance of cells due to the low autophagic response that poses detrimental effects in mutated fibroblasts. This hypothesis is further supported by the fibroblast CMT2A^{MFN2} transcriptomic profile that revealed a down-regulation of RAB37, which was shown to affect the formation of the complex (ATG5–12/ATG16L1) regulating the LC3B lipidation (103). It would be worth investigating if the reduced conversion of LC3B-I to LC3B-II is to be associated with the reduced RAB37 expression. In addition, mito-derived phosphatidylethanolamine (PtdEtn) (from mitochondria at MAM) is known to produce membrane-associated to the LC3B-II and the PtdIns3P-enriched subdomains of the ER (*omegasomes*) (104), therefore reduced MAM could be the cause of reduced autophagy. Importantly, previous findings have suggested that *MFN2* can participate directly in the maturation of autophagosome membranes because of its localization at ER membrane from which they originate (105–109). Selective mitochondrial autophagy, or mitophagy, defines the quality control pathway that operates the removal of non-functional or damaged mitochondria (110). Mitophagy specifically targets mitochondria to autophagosomes for subsequent degradation in lysosomes; the induction of the autophagy machinery is fundamental for the removal of depolarized and isolated (by fission) mitochondria (111). In mammals, it involves PINK1 and PRKN (112,113). MFN2 plays a role as an intermediate molecule in signaling between mitochondrial PINK1 kinase and cytosolic PRKN as observed in neurons and cardiomyocytes (114–118). In short, the PINK1 kinase is actively imported into the mitochondria where, under normal conditions, is immediately degraded by PARL proteolysis. Therefore, healthy mitochondria contain little or no PINK1 protein. However, PINK1 degradation is suppressed in damaged/stressed/depolarized mitochondria, allowing the accumulation of PINK1. When present, PINK1 phosphorylates numerous mitochondrial substrates, including MFN2 at least at three positions (43,115). The phosphorylation of MFN2 by PINK1 promotes MFN2-Parkin binding on the outer mitochondrial membrane, facilitating PRKN-mediated ubiquitination of one hundred outer membrane proteins (119). PINK1-phosphorylated MFN2 is not only a 'PRKN receptor,' but it loses the ability to promote mitochondrial fusion (43,115). Ubiquitinated mitochondrial outer membrane proteins attract autophagosomes and stimulate autophagosome embedding in the damaged organelle, thus initiating mitophagy (113). When we investigated mitophagy mitochondrial markers in CMT2A^{MFN2} fibroblasts, we found normal PINK1/PRKN colocalization, suggesting that *MFN2* mutation does not affect the mitophagy protein recruitment on defective mitochondria. Such mitochondria are efficiently recruited to form the mitophagosomes although a lower number of autophagosomes are present in CMT2A^{MFN2} cells. Despite the low autophagic response, we did not find an accumulation of mitochondria within CMT2A^{MFN2} cells that led us to hypothesize the induction of an alternative pathway to clear the cells from damaged mitochondria. To elucidate these and other molecular pathways perturbed in mutated CMT2A^{MFN2} fibroblasts, we performed a whole RNA sequencing of CMT2A and control fibroblasts. DEGs were mainly enriched in the PBs and MCs involved in cell adhesion, extracellular matrix organization, and positive regulation of cell proliferation. In addition, PPI showed good connectivity between the DEG, and the primary clusters of the PPI network were also enriched in cell-cycle processes, cell–substrate adhesion and cell–matrix adhesion. Consistently with our work, similar deregulated pathways have been detected in RNAseq data from CMT2A patient-derived motor neurons in which depleted genes were associated with extracellular matrix function (44).

Transcripts encoding key factors involved in positive regulation of phosphatidylinositol 3-kinase (PtdIns3K) signaling, which acts upstream mTOR, were also significantly altered. We found differential expression in genes encoding proteins that negatively regulate mTORC (i.e. DEPTOR, SESN2), and EIF4EBP1, one of the major substrates of mTORC1. IGF1 expression was significantly increased (3.73-fold change). Also, IGF1 can inhibit autophagy via activation of mTORC2 and directly AKT, which represent mTORC1-independent signaling (114). Investigating the activation of AKT, we observed a strong increase of mTORC2-dependent phosphorylation of AKT(Ser473) in mutant fibroblasts. In agreement with the known anabolic effects of PtdIns3K/AKT/mTORC pathway activation, the CMT2A^{MFN2} fibroblasts showed a remarkable decrease in autophagy and increase in cell proliferation. Pharmacologic treatment of AKT allowed us to prove that AKT can be targeted to restore autophagy and cell proliferation rate in CMT2A^{MFN2} cells (Fig. 7). Interestingly, in rat vascular smooth muscle cells, AKT signaling—which is to act through both a

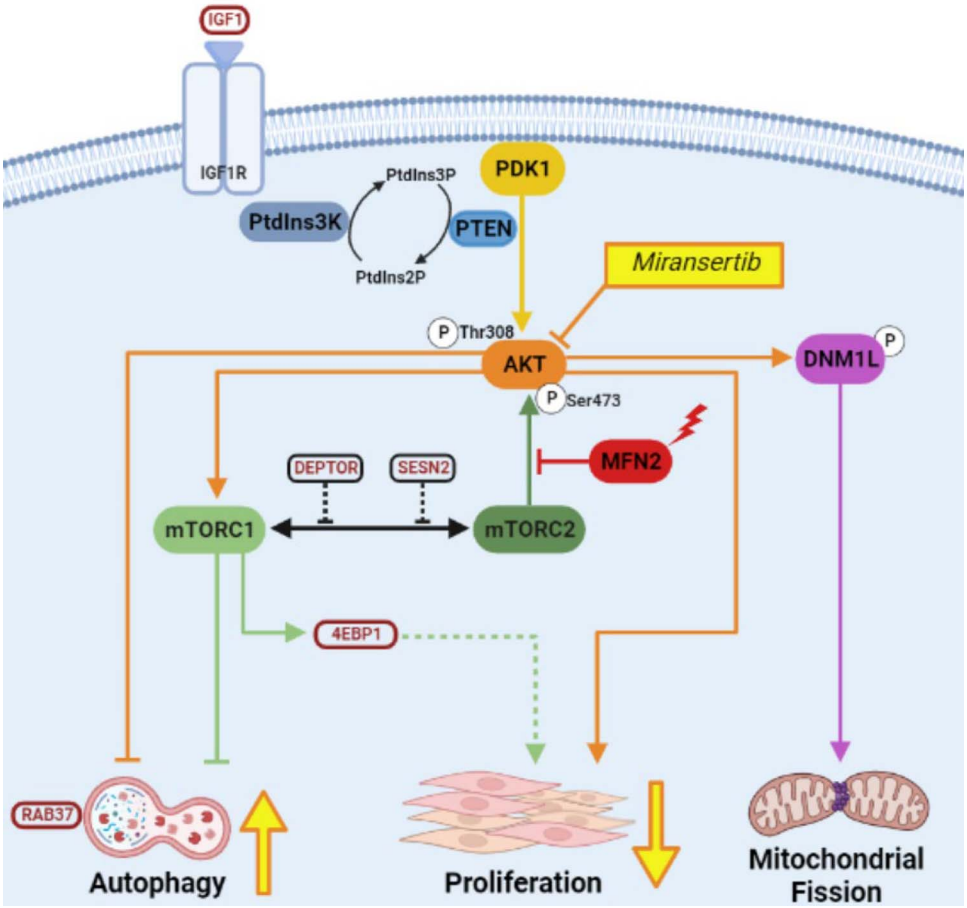

Figure 7. Schematic representation of the altered processes in CMT2A^{MFN2} fibroblasts. The phosphatidylinositol 3-kinase (PtdIns3K) catalyzes the phosphorylation of the phosphatidylinositol 4,5-bisphosphate (PtdIns2P) to phosphatidylinositol-3,4,5-trisphosphate (PtdIns3P) and this activity is reversed by PTEN. PtdIns3P recruits several proteins to the membrane, including 3-phosphoinositide-dependent kinase (PDK1) that phosphorylates AKT at Thr(308). A second AKT phosphorylation, required for its complete activation, is operated by mTORC2 at Ser(473) leading to cellular proliferation. This mTORC2 kinase activity is suppressed by the interaction with MFN2. AKT can: activate cellular proliferation either directly or via mTORC1 that acts on 4E-BP1; inhibit autophagy either by a mTORC1-dependent or by an independent regulation; promote mitochondrial fission by DNM1L phosphorylation. Miransertib, an AKT inhibitor, has been highlighted in yellow as well as the two arrows indicating its effects on autophagy and cell proliferation. Circles with red names indicate DEGs found in CMT2A^{MFN2} fibroblasts: IGF-1, SESN2, DEPTOR (negative regulators of mTORC) and EIF4EBP1 (4EBP1 is the protein name). Interestingly, IGF1 is an activator of the PtdIns3K/AKT/mTORC pathway.

mTORC1 dependent (54) and independent (120–123) regulation—was reported as a target of regulation by *MFN2*, by suppressing mTORC2 which promotes cancer cell growth and metastasis via the AKT(Ser473) phosphorylation mediated signaling pathway (17).

Previous studies indicate that AKT in turn regulates mitochondrial dynamics, directly activating DNM1L and promoting mitochondrial fission (124). We investigated the DNM1L expression that was found enhanced in CMT2A^{MFN2} fibroblasts. Although we did not test the phosphorylation state of this protein, we cannot exclude that the presence of a fragmented mitochondrial network morphology in CMT2A^{MFN2} fibroblasts could be a consequence of mitochondria hyper-fission driven by DNM1L rather than a consequence of fusion inhibition (30,32). Since AKT activation is regulated by *MFN2* itself through mTORC2 activation, we can argue that MFN2 mutation drives these aspects. Despite the loss of mitochondrial transmembrane potential, the mitochondrial fragmentation state, and the reduced stimulus to induction of autophagy, the finding that CMT2A^{MFN2} fibroblasts display increased mitotic rate suggests that mitochondrial impairment exerts a pro-survival role.

In summary, here we demonstrated that human CMT fibroblasts harboring heterozygous single nucleotide substitution c.650G > T in *MFN2*, decreased autophagy and increased cell proliferation can be attenuated by inhibiting AKT (Fig. 7). Therefore, this work unveiled a novel potential role of the mTOR/AKT pathway in CMT2A2 pathophysiology.

We are aware that our study presents several limitations including low sample size and that the data derived could be due to the specific genetic variant or its background. Nevertheless, the involvement of the *MFN2* gene in cell proliferation presented either in the *mfn2* KO animal model or in tumor cells supports the role of *MFN2* in cell proliferation that has never been reported in CMT2A cells. At least three questions remain open that would be worth exploring: 1. whether the reduction of autophagy and the acceleration in cell division rate occurs in neuronal committed cells from CMT2A patients; 2. why apoptosis is not activated; 3. if a metabolic shift occurs towards more anaerobic metabolism. Further investigations on the role of the targets uncovered by our analysis will require appropriate models for validation (i.e. in vitro co-cultures, MFN2 knock-in mouse model) and are beyond the scope of this study.

Materials and Methods

Cell culture and analysis

Primary fibroblasts from a young patient affected by CMT2A^{MFN2} (c.650G > T/p.Cys217Phe) and a healthy 11 years-old girl (individual with no histological or biochemical signs of mitochondrial disease), were obtained by explants from skin punch biopsy, after informed consent. Cells were grown in high-glucose Dulbecco's modified Eagle's medium (DMEM; EuroClone, ECB7501LX10) supplemented with 10% (v/v) fetal bovine serum (FBS; EuroClone, ECS5000L), 1% (v/v) L-glutamine (E EuroClone, ECB3000D), 1% (v/v) penicillin/streptomycin (EuroClone, ECB3001D), 50 μg/ml of uridine (Sigma-Aldrich, U3003), at 37°C in a humidified atmosphere of 5% CO_2. All experiments were performed on cells with similar passage numbers, ranging from 3 to 14, to avoid an artifact due to senescence. For the experiments, growing cells were plated on sterile plastic dishes, on sterile plastic flasks, or sterile glass coverslips and allowed to adhere for at least 24 h before use.

For mitochondrial network studies, where indicated, cells were grown in DMEM lacking glucose supplemented with 5.5 mM of galactose (DMEM galactose) for 72 h. For inhibition of autophagy, CQ (C6628) was added to the cell culture medium at a concentration of 50 μM, whereas to induce autophagy, Torin1 (475991) was added at concentrations of 1 μM. CQ and Torin1 were added for 3 h before the end of the treatments. For mitochondrial network and mitophagy studies, the uncoupler agent carbonyl cyanide p-(trifluoromethoxy) phenylhydrazone (CCCP; C2920) was used at 10 μM for 4 h. These chemicals were purchased from Sigma-Aldrich unless otherwise indicated. Miransertib (MedChemExpress, USA) was used at a concentration of 1 μM for 72 h, and DMSO as a vehicle (125).

Mitochondrial DNA analysis

Total DNA (nuclear and mitochondrial) was extracted from patient-derived fibroblasts and control fibroblasts using the 'Wizard® Genomic DNA Purification Kit' (Promega, A1125) according to the manufacturer's instructions. DNA yield was determined using the ND-1000 Spectrophotometer (NanoDrop; Thermo Fisher Scientific, MA, USA), whereas the integrity and quality of the DNA were evaluated on 0.8% agarose gel. As described previously, large-scale mitochondrial deletions detection was performed by long-range PCR (126). Long-range PCR was performed using F500, 5'-CCCATCCTACCCAGCACACA-3'and R11, 5'-CGTGAGTGGTTAATAGGGTGATAGACCTG-3′ as specific mtDNA primers. Mitochondrial DNA copy number was measured using quantitative real-time PCR, as described previously (127). In brief, MT-ND1, as mtDNA target, and beta-2-microglobulin (B2M), as a reference for the nuclear DNA content, were amplified using the LightCycler 480 Sybr Green I Master Mix (Thermo Fisher, 4309155) according to the manufacturer's instruction and reactions were performed on the Light Cycler 480 (Roche, Switzerland) instrument. The primer pairs used for quantitative real-time PCR were: ND1-F, 5'-GAAGTCACCCTAGCCATCATTC-3′; ND1-R, 5'-GCAGGAGTAATCAGAGGTGTTC-3′; B2M-F, 5'-ACCTCC ATGATGCTGCTTAC-3′; 5'-GGACTGGTCTTTCTATCTCTTGTAC-3′. The mtDNA copy number was calculated by using the $2^{-\Delta Ct}$ method, and values were divided by the number of nuclear copies of B2M to calculate the effective mtDNA content per cell.

Oxygen electrode polarography

Mitochondrial oxygen consumption was measured in intact exponentially growing cells using a Clark-type oxygen electrode in a water-jacketed chamber (Oxygraph; Hansatech Instruments, England), magnetically stirred at 37°C. Cells, fluid changed the day before, were collected by trypsinization and centrifugation, washed once in TD buffer (0.137 M NaCl, 5 mM KCl, 0.7 mM Na2HPO4, 25 mM Tris–HCl, pH 7.4), resuspended in the same buffer, previously air equilibrated at 37°C, and transferred into a polarographic chamber, at a final concentration of 1 x 10^6 cells per ml; aliquots were used for cell counting and protein determination. The chamber was stoppered. After the native endogenous O_2 consumption rate was recorded, dinitrophenol (DNP; D198501) was added and substrate-driven respiration rates were measured in digitonin-permeabilized cells, as described (128). Briefly, respiratory substrates and inhibitors were added at the following concentrations: 5 mM glutamate (RES5063G-A701X)/2.5 mM malate (M1000), 5 mM succinate (W327700) in the presence of 200 nM rotenone (R8875) and 10 mM ascorbate (A7631) + 0.4 mM (N, N, N′, N′-tetramethyl-p-phenylenediamine (TMPD; T3134) in the presence of 15 nM antimycin A (A8674) for Complex I (CI)-, Complex II (CII)- and Complex IV (CIV)-driven respiration, respectively. All chemicals were purchased from Sigma-Aldrich.

Western blotting analysis

Fibroblasts were collected at the confluence, washed twice with Dulbecco's Phosphate Buffered Saline 10X (DPBS; Euroclone, ECB4004L), and then homogenized in RIPA buffer (ThermoFisher Scientific, 89900) containing inhibitors of proteases (Cell Signaling, 5871), following standard protocols. The cells were sonicated on ice, centrifuged for 10 min at 16 000 × g at 4°C and the protein concentrations were determined by Bradford assay (Bio-Rad, 500-0006). About 20–50 μg of cell proteins were lysed and denatured in Laemmli Buffer 2X (Bio-Rad, 1610737), separated by Sodium Dodecyl Sulfate-Polyacrylamide Gel Electrophoresis (SDS-PAGE) using homemade 8% or 10% separating gel or 12% TGX Stain-Free FastCast Gels (Bio-Rad, 1 610 185) and then transferred onto Polyvinylidene Fluoride (PVDF) membranes using a Trans-Blot transfer apparatus (Bio-Rad, California, USA). To avoid non-specific binding, membranes were blocked with Tris-Buffered Saline (TBS) (20 mM Tris base, 150 mM NaCl)/0.1%-Tween20 (BioRad, 1706531) Tween-Tris-Buffered Saline (TTBS) containing 5% non-fat dry milk before overnight incubation with the specified antibodies. Primary antibodies were incubated overnight at 4°C in TTBS with 2.5% non-fat dry milk, and those not bound specifically were removed by washing in TTBS. The following primary antibodies were used: anti-p62 (SQSTM1, BD Transduction Laboratories, 610833); anti-LC3B (Sigma-Aldrich, L7543) for autophagy flux study; anti-MFN2 (Abnova, H00009927), anti-OPA1 (BD Transduction Laboratories, 612606) and anti-DRP1 (DNM1L, Santa Cruz Biotechnology, sc-271 583) for the study of mitochondrial dynamics machinery. The phosphorylation level of AKT on Thr308 and Ser473 was measured with phospho-specific antibodies (Cell Signaling Technology, D25E6, D95, respectively) and adjusted to total AKT using an AKT total antibody (Cell Signaling Technology, 40D4) (Supplementary Material, Table S4). Membranes were then re-probed with an antibody specific for GAPDH (ProteinTech, 60 004-1-Ig) as an index of homogenate protein loading in the lanes. Peroxidase affinity pure goat anti-mouse IgG and goat anti-rabbit IgG (Bio-Rad, 1706 516 and 1706515, respectively) were added for 1 h at room temperature in the same buffer used for the primary antibodies (2.5% non-fat dry milk in TTBS). According to the manufacturer's instructions, reactive bands were detected using Clarity Western ECL Substrate (Bio-Rad, 1705061). Image acquisition was performed by the LI-COR C-Digit blot scanner and densitometric analysis was performed by the Image Studio Acquisition software (Licor, Lincoln, NE).

Immunofluorescence assays

The following primary antibodies were used: anti-VDAC1/Porin antibody (Abcam, ab15895) for mitochondrial network morphology study; anti-p62 (SQSTM1, BD Transduction Laboratories, 610 833); anti-LC3B (Sigma-Aldrich, L7543); anti-Human LAMP1 (BD Pharmingen, 555 798) anti-TOMM20 (Abcam, ab56783); anti-PINK1(Abcam, EPR20730) and anti-Parkin (PRKN=PRK8) (Santa Cruz Biotechnology, sc-32 282) for autophagy/mitophagy study (Supplementary Material, Table S4). After three washes in PBS, cells were reacted with appropriate secondary antibodies conjugated with Alexa Fluor 488 or 568 (ThermoFisher Scientific, A11001 and A11036, respectively) for 1 h at room temperature in a humid chamber. Nuclear chromatin was stained with the fluorescent dye 4,6-diamidino-2-phenylindole-dihydrochloride 5 μg/ml (DAPI; Sigma-Aldrich, D9542) for 10 min at room temperature and, after three washes in PBS, coverslips were mounted in Vectashield (Vector, H-100-10). Stained cells were examined with a Nikon Ti2-E inverted microscope (Nikon, Japan) or with an Olympus photomicroscope (Olympus, Center Valley, PA) or with a Leica TCS SP8 microscope (Leica Microsystems, Buffalo Grove, IL, USA) coupled to the laser scanning confocal microscopy (LSCM) system.

Structural changes to mitochondria were analyzed upon staining with MitoTracker Red (Invitrogen, Carlsbad, CA, USA), 500 nM for 30 min at 37°C. Images were acquired at 60x magnifications (Nikon×60 Plan Apocr λ NA = 1.40 oil immersion objective) with a Nikon Ti2-inverted microscope equipped with a structured illumination imaging systeM ViCo 2.0. We outlined three different mitochondrial morphology groups: tubular mitochondria (circularity 0–0.3), intermediate mitochondria (circularity 0.3–0.6) and fragmented mitochondria (circularity 0.6–1) as described elsewhere (129). Mitochondrial circularity was quantified by using ImageJ software (https://imagej.nih.gov/ij/). For each experiment, at least 20 cells were used to calculate the relative percentages of the mitochondrial areas for the different mitochondrial groups normalized on the total area of the mitochondrial compartment.

For mitophagy analysis, stained cells were examined with a Leica TCS SP8 microscope coupled to the LSCM system, using 40x and 63× oil immersion objectives with a pinhole airy unit of 1. Dots counting was performed using the default 'analyze particles' plugin in ImageJ software. Optical Z of the cells was taken by a threshold intensity, binary images were obtained. Puncta with area of 0.1–1.767 um^2 were quantitated for LC3B; 0.03–0.5 um^2 for LAMP1; 0.75–3 um^2 for TOMM20; > 0.08 um^2 for PINK1 and PRKN.

Colocalization measurement was obtained by counting the dots occupied by the overlapping element for the cell (i.e. LPrc; PPrc) or by the ratio between the dots occupied by the overlapping element and single-channel dots (i.e. LTc: T; LLpc: Lp; PTc:P). At least 30 cells were measured.

JC-1 staining of mitochondria in fibroblasts

Detection of altered mitochondrial membrane potential ($\Delta\psi m$) was performed using the 5,5′,6,6′-tetrachloro-1,1′,3,3′ tetraethylbenzimidazolylcarbocyaniniodidee (JC-1) dye (Invitrogen, T3168), according to the protocol described by Chazotte (130). Cultured fibroblasts grown on a sterile coverslip in a 6-well plate, were incubated with 10 µg/ml of JC-1 in the dark for 15 min at 37°C, 5% CO2 before analysis. Cells were then washed three with a culture medium, fixed with 4% PFA, counterstained with 5 μg/ml of DAPI, and mounted in Vectashield (Vector). For each independent experiment, the intensity of the signal was analyzed in more than 30 cells. Images were obtained by Olympus photomicroscope (Olympus, Center Valley, PA) with a 40x objective lens. The integrated density of red and green channels for each cell was measured using ImageJ software and the red/green intensity ratio was calculated considering that high mitochondrial membrane potential is associated with red JC-1 emission.

Growth curves and doubling time of CMT2A^{MFN2} and control fibroblasts

The doubling time of CMT2A^{MFN2} fibroblasts in 10% FBS supplemented DMEM was calculated by cell counting method and using the following formula: PD = t x Log2/(LogC2-LogC1). [PD = Population doubling time, t = 24 hours (interval of cell count), Log = 10 based Log, C1 = 1st cell count, C2 = 2nd cell count]. For calculation of doubling time in 10% FBS supplemented DMEM, CMT2A^{MFN2} fibroblasts and control cells were seeded in 24-well plates and grown for 5 days in normal culture conditions. Cells were harvested by trypsinization and counted by hemocytometer every 24 h from day 1 to day 5. PD time was calculated every 24 h using the above formula from day 0 to day 1. The main PD was determined. To evaluate the antiproliferative effect of the AKT inhibitor Miransertib, CMT2A^{MFN2} fibroblasts and control cells were seeded in 24-well plates and grown for 3 days in both Miransertib and vehicle treatment conditions. Cells were harvested by trypsinization and counted by hemocytometer every 24 h from day 1 to day 3. Cells were examined with Zeiss Primovert (Zeiss, Germany). A total of three individual experiments were performed (131).

Preprocessing and analysis of RNA-Seq read

RNA was extracted from CMT2A^{MFN2} fibroblasts and controls fibroblasts using the RNeasy Plus Kit (Qiagen, 74034) according to the manufacturer's instructions. Each RNA sample was qualitatively and quantitatively checked on Agilent 2100 Bioanalyzer RNA Nano Chip (Agilent, Santa Clara, CA, USA). Directional RNA-Seq libraries were prepared from 100 ng of total RNA using the TruSeq Stranded Total RNA Sample Prep Kit (Illumina, 20020597) according to the manufacturer's protocol. Sequencing was performed on an Illumina NextSeq 500 platform (Illumina, San Diego, CA).

RNA-Seq reads in FASTQ format were initially inspected using the FASTQC program (http://www.bioinformatics.babraham.ac.uk/projects/fastqc/). Adaptors and low-quality regions (Phred cut-off of 20) were trimmed using fastp (132), excluding reads with a final length of fewer than 50 bases. Cleaned reads were aligned onto the complete human genome (assembly hg38) using STAR (133) and providing a list of exon-exon junctions from GENCODE. The generalized fold change algorithm (GFOLD) was used to assign reads to known human annotations and perform differential gene expression. We considered only genes with a GFOLD (adjusted log2 fold change) value equal to or higher than 1.5 in absolute value. Functional annotation of DEG was conducted with the online software DAVID (https://david.ncifcrf.gov/tools.jsp, 2021 Update). The software systematically extracts biological information from numerous genes and performs GO (www.geneontology.org) enrichment covering three aspects of biology: biological processes (BP), cellular components (CC) and molecular functions (MF). Furthermore, the software also performs Kyoto Encyclopedia of Genes and Genomes (KEGG; www.genome.jp/) pathway analysis. Functional and pathway enrichment analyses were selected with a Benjamini-Hochberg false discovery rate (FDR) $P < 0.001$. String (https://string-db.org/) was used to evaluate PPI between DEGs and networks were constructed with

STRINGApp on Cytoscape software (Version: 3.9.1) (134) with a cut-off confidence score of 0.8. To further analyze the physical relationships among DEGs, the Cytoscape plug-in molecular complex detection (MCODE, version 2.0.0; http://apps.cytoscape.org/apps/mcode) identifies the most important sub-modules of the network map. The criteria of MCODE analysis were degree cut-off = 2, MCODE score > 5, Max depth = 100, node score cut-off = 0.2 and *k*-score = 2. The Biological Networks Gene Ontology tool (BiNGO, version 3.0.3; http://apps.cytoscape.org/apps/bingo) was used to analyze and visualize the biological processes of identified sub-modules with an FDR corrected *P*-value < 0.001.

cDNA synthesis and Sanger sequencing

cDNA was synthesized using QuantiTect® Reverse Transcription Kit (Qiagen, 205 311) according to the manufacturer's protocol. Polymerase chain reaction (PCR) was performed to amplify a specific region including the mutation, with the following primers: forward 5′-AGGGCTCAGAGGAAAAGAGG-3′ and reverse 5′-AGACGCTCACTCACCTTGTG-3′. A 298 bp PCR product was purified using PureLink™ PCR Purification Kit (Invitrogen, K3 100-01) and analyzed by Sanger Sequencing at Microsynth Seqlab GmbH (Göttingen, Germany).

Statistical analysis

All statistical analyses were performed using PRISM® 7.04 in analytical software (GraphPad Software Inc, San Diego, CA) and Excel (Microsoft, Inc.). Results were expressed as average values ± SD of at least three independent determinations, each performed in triplicate, if not otherwise specified using sex and age-matched control and CMT2A^{MFN2} fibroblasts. Statistical significance was calculated using Student's *t* parametric test set at: $^{*}P < 0.05$; $^{**}P < 0.01$; and $^{***}P < 0.001$; and $^{****}P < 0.0001$. One-way analysis of variance (ANOVA) test was performed to examine the differences between more than two dependent groups. The Bonferroni correction was used for multiple comparisons.

Supplementary Material

Supplementary Material is available at *HMGJ* online.

Acknowledgements

We thank the family for participating in this study, the patients' associations MITOCON, UILDM (Unione Italiana Lotta alla Distrofa Muscolare), and CollaGe-Associazione-Genitori-Manzoni-Poli-Molfetta. We thank Prof. Gennaro Agrimi (University of Bari) for helpful suggestions and Prof. Nicoletta Resta (University of Bari) for her support.

Conflict of Interest statement. None declared.

Funding

REGIONE PUGLIA-MALATTIE RARE-Petruzzella (Del. N.246 10.09. 2019_UPB-SMBNOS) and by donations of Parents' Associations including UILDM and CollaGe (to V.P.) and Opera Pia Foundation (to P.Z. and A.A.). Financial support from the Italian Ministry of Health-Ricerca Corrente (2021- 5X1000 to S.D. and F.M.S.).

Disclosure statement

All authors have read and agreed to the published version of the manuscript. The authors alone are responsible for the content and writing. No potential competing interest was reported by the authors.

References

1. Sabouny, R. and Shutt, T.E. (2020) Reciprocal regulation of mitochondrial fission and fusion. *Trends Biochem. Sci.*, **45**, 564–577.
2. Sugiura, A., McLelland, G.-L., Fon, E.A. and McBride, H.M. (2014) A new pathway for mitochondrial quality control: mitochondrial-derived vesicles. *EMBO J.*, **33**, 2142–2156.
3. Lackner, L.L. (2019) The expanding and unexpected functions of mitochondria contact sites. *Trends Cell Biol.*, **29**, 580–590.
4. Onishi, M., Yamano, K., Sato, M., Matsuda, N. and Okamoto, K. (2021) Molecular mechanisms and physiological functions of mitophagy. *EMBO J.*, **40**, e104705.
5. Chen, H., McCaffery, J.M. and Chan, D.C. (2007) Mitochondrial fusion protects against neurodegeneration in the cerebellum. *Cell*, **130**, 548–562.
6. Chen, H., Vermulst, M., Wang, Y.E., Chomyn, A., Prolla, T.A., McCaffery, J.M. and Chan, D.C. (2010) Mitochondrial fusion is required for mtDNA stability in skeletal muscle and tolerance of mtDNA mutations. *Cell*, **141**, 280–289.
7. Chen, Y., Liu, Y. and Dorn, G.W. (2011) Mitochondrial fusion is essential for organelle function and cardiac homeostasis. *Circ. Res.*, **109**, 1327–1331.
8. Koshiba, T., Detmer, S.A., Kaiser, J.T., Chen, H., McCaffery, J.M. and Chan, D.C. (2004) Structural basis of mitochondrial tethering by mitofusin complexes. *Science*, **305**, 858–862.
9. Chen, H. and Chan, D.C. (2009) Mitochondrial dynamics–fusion, fission, movement, and mitophagy–in neurodegenerative diseases. *Hum. Mol. Genet.*, **18**, R169–R176.
10. Franco, A., Kitsis, R.N., Fleischer, J.A., Gavathiotis, E., Kornfeld, O.S., Gong, G., Biris, N., Benz, A., Qvit, N., Donnelly, S.K. *et al.* (2016) Correcting mitochondrial fusion by manipulating mitofusin conformations. *Nature*, **540**, 74–79.
11. Mattie, S., Riemer, J., Wideman, J.G. and McBride, H.M. (2018) A new mitofusin topology places the redox-regulated C terminus in the mitochondrial intermembrane space. *J. Cell Biol.*, **217**, 507–515.
12. Thaher, O., Wolf, C., Dey, P.N., Pouya, A., Wüllner, V., Tenzer, S. and Methner, A. (2018) The thiol switch C684 in Mitofusin-2 mediates redox-induced alterations of mitochondrial shape and respiration. *Neurochem. Int.*, **117**, 167–173.
13. Hernández-Alvarez, M.I., Thabit, H., Burns, N., Shah, S., Brema, I., Hatunic, M., Finucane, F., Liesa, M., Chiellini, C., Naon, D. *et al.* (2010) Subjects with early-onset type 2 diabetes show defective activation of the skeletal muscle PGC-1{alpha}/Mitofusin-2 regulatory pathway in response to physical activity. *Diabetes Care*, **33**, 645–651.
14. Bach, D., Pich, S., Soriano, F.X., Vega, N., Baumgartner, B., Oriola, J., Daugaard, J.R., Lloberas, J., Camps, M., Zierath, J.R. *et al.* (2003) Mitofusin-2 determines mitochondrial network architecture and mitochondrial metabolism. A novel regulatory mechanism altered in obesity. *J. Biol. Chem.*, **278**, 17190–17197.
15. Chen, K.-H., Guo, X., Ma, D., Guo, Y., Li, Q., Yang, D., Li, P., Qiu, X., Wen, S., Xiao, R.-P. *et al.* (2004) Dysregulation of HSG triggers vascular proliferative disorders. *Nat. Cell Biol.*, **6**, 872–883.
16. Zhang, G.-E., Jin, H.-L., Lin, X.-K., Chen, C., Liu, X.-S., Zhang, Q. and Yu, J.-R. (2013) Anti-tumor effects of Mfn2 in gastric cancer. *Int. J. Mol. Sci.*, **14**, 13005–13021.
17. Xu, K., Chen, G., Li, X., Wu, X., Chang, Z., Xu, J., Zhu, Y., Yin, P., Liang, X. and Dong, L. (2017) MFN2 suppresses cancer progres-

sion through inhibition of mTORC2/Akt signaling. *Sci. Rep.*, **7**, 41718.
18. Rocha, N., Bulger, D.A., Frontini, A., Titheradge, H., Gribsholt, S.B., Knox, R., Page, M., Harris, J., Payne, F., Adams, C. *et al.* (2017) Human biallelic MFN2 mutations induce mitochondrial dysfunction, upper body adipose hyperplasia, and suppression of leptin expression. *elife*, **6**, e23813.
19. Capel, E., Vatier, C., Cervera, P., Stojkovic, T., Disse, E., Cottereau, A.-S., Auclair, M., Verpont, M.-C., Mosbah, H., Gourdy, P. *et al.* (2018) MFN2-associated lipomatosis: clinical spectrum and impact on adipose tissue. *J. Clin. Lipidol.*, **12**, 1420–1435.
20. Züchner, S., Mersiyanova, I.V., Muglia, M., Bissar-Tadmouri, N., Rochelle, J., Dadali, E.L., Zappia, M., Nelis, E., Patitucci, A., Senderek, J. *et al.* (2004) Mutations in the mitochondrial GTPase mitofusin 2 cause Charcot-Marie-Tooth neuropathy type 2A. *Nat. Genet.*, **36**, 449–451.
21. Bombelli, F., Stojkovic, T., Dubourg, O., Echaniz-Laguna, A., Tardieu, S., Larcher, K., Amati-Bonneau, P., Latour, P., Vignal, O., Cazeneuve, C. *et al.* (2014) Charcot-Marie-Tooth disease type 2A: from typical to rare phenotypic and genotypic features. *JAMA Neurol.*, **71**, 1036–1042.
22. Choi, B.-O., Nakhro, K., Park, H.J., Hyun, Y.S., Lee, J.H., Kanwal, S., Jung, S.-C. and Chung, K.W. (2015) A cohort study of MFN2 mutations and phenotypic spectrums in Charcot-Marie-Tooth disease 2A patients. *Clin. Genet.*, **87**, 594–598.
23. Fridman, V., Bundy, B., Reilly, M.M., Pareyson, D., Bacon, C., Burns, J., Day, J., Feely, S., Finkel, R.S., Grider, T. *et al.* (2015) CMT subtypes and disease burden in patients enrolled in the Inherited Neuropathies Consortium natural history study: a cross-sectional analysis. *J. Neurol. Neurosurg. Psychiatry*, **86**, 873–878.
24. Ando, M., Hashiguchi, A., Okamoto, Y., Yoshimura, A., Hiramatsu, Y., Yuan, J., Higuchi, Y., Mitsui, J., Ishiura, H., Umemura, A. *et al.* (2017) Clinical and genetic diversities of Charcot-Marie-Tooth disease with MFN2 mutations in a large case study. *J. Peripher. Nerv. Syst.*, **22**, 191–199.
25. Hoebeke, C., Bonello-Palot, N., Audic, F., Boulay, C., Tufod, D., Attarian, S. and Chabrol, B. (2018) Retrospective study of 75 children with peripheral inherited neuropathy: genotype-phenotype correlations. *Arch. Pediatr.*, **25**, 452–458.
26. Yoshimura, A., Yuan, J.-H., Hashiguchi, A., Ando, M., Higuchi, Y., Nakamura, T., Okamoto, Y., Nakagawa, M. and Takashima, H. (2019) Genetic profile and onset features of 1005 patients with Charcot-Marie-Tooth disease in Japan. *J. Neurol. Neurosurg. Psychiatry*, **90**, 195–202.
27. Feely, S.M.E., Laura, M., Siskind, C.E., Sottile, S., Davis, M., Gibbons, V.S., Reilly, M.M. and Shy, M.E. (2011) MFN2 mutations cause severe phenotypes in most patients with CMT2A. *Neurology*, **76**, 1690–1696.
28. Stuppia, G., Rizzo, F., Riboldi, G., Del Bo, R., Nizzardo, M., Simone, C., Comi, G.P., Bresolin, N. and Corti, S. (2015) MFN2-related neuropathies: clinical features, molecular pathogenesis and therapeutic perspectives. *J. Neurol. Sci.*, **356**, 7–18.
29. Guerriero, S., D'Oria, F., Rossetti, G., Favale, R.A., Zoccolella, S., Alessio, G. and Petruzzella, V. (2020) CMT2A harboring mitofusin 2 mutation with optic nerve atrophy and normal visual acuity. *Int. Med. Case Rep. J.*, **13**, 41–45.
30. Amiott, E.A., Lott, P., Soto, J., Kang, P.B., McCaffery, J.M., DiMauro, S., Abel, E.D., Flanigan, K.M., Lawson, V.H. and Shaw, J.M. (2008) Mitochondrial fusion and function in Charcot-Marie-Tooth type 2A patient fibroblasts with mitofusin 2 mutations. *Exp. Neurol.*, **211**, 115–127.
31. Vielhaber, S., Debska-Vielhaber, G., Peeva, V., Schoeler, S., Kudin, A.P., Minin, I., Schreiber, S., Dengler, R., Kollewe, K., Zuschratter, W. *et al.* (2013) Mitofusin 2 mutations affect mitochondrial function by mitochondrial DNA depletion. *Acta Neuropathol.*, **125**, 245–256.
32. Loiseau, D., Chevrollier, A., Verny, C., Guillet, V., Gueguen, N., Pou de Crescenzo, M.-A., Ferré, M., Malinge, M.-C., Guichet, A., Nicolas, G. *et al.* (2007) Mitochondrial coupling defect in Charcot-Marie-Tooth type 2A disease. *Ann. Neurol.*, **61**, 315–323.
33. Guillet, V., Gueguen, N., Cartoni, R., Chevrollier, A., Desquiret, V., Angebault, C., Amati-Bonneau, P., Procaccio, V., Bonneau, D., Martinou, J.-C. *et al.* (2011) Bioenergetic defect associated with mKATP channel opening in a mouse model carrying a mitofusin 2 mutation. *FASEB J.*, **25**, 1618–1627.
34. Baloh, R.H., Schmidt, R.E., Pestronk, A. and Milbrandt, J. (2007) Altered axonal mitochondrial transport in the pathogenesis of Charcot-Marie-Tooth disease from mitofusin 2 mutations. *J. Neurosci.*, **27**, 422–430.
35. Misko, A.L., Sasaki, Y., Tuck, E., Milbrandt, J. and Baloh, R.H. (2012) Mitofusin2 mutations disrupt axonal mitochondrial positioning and promote axon degeneration. *J. Neurosci.*, **32**, 4145–4155.
36. Chan, D.C. (2012) Fusion and fission: interlinked processes critical for mitochondrial health. *Annu. Rev. Genet.*, **46**, 265–287.
37. Detmer, S.A. and Chan, D.C. (2007) Complementation between mouse Mfn1 and Mfn2 protects mitochondrial fusion defects caused by CMT2A disease mutations. *J. Cell Biol.*, **176**, 405–414.
38. Zhou, Y., Carmona, S., Muhammad, A.K.M.G., Bell, S., Landeros, J., Vazquez, M., Ho, R., Franco, A., Lu, B., Dorn, G.W. *et al.* (2019) Restoring mitofusin balance prevents axonal degeneration in a Charcot-Marie-Tooth type 2A model. *J. Clin. Invest.*, **129**, 1756–1771.
39. de Brito, O.M. and Scorrano, L. (2008) Mitofusin 2 tethers endoplasmic reticulum to mitochondria. *Nature*, **456**, 605–610.
40. Naon, D., Zaninello, M., Giacomello, M., Varanita, T., Grespi, F., Lakshminaranayan, S., Serafini, A., Semenzato, M., Herkenne, S., Hernández-Alvarez, M.I. *et al.* (2016) Critical reappraisal confirms that Mitofusin 2 is an endoplasmic reticulum-mitochondria tether. *Proc. Natl. Acad. Sci. U. S. A.*, **113**, 11249–11254.
41. Larrea, D., Pera, M., Gonnelli, A., Quintana-Cabrera, R., Akman, H.O., Guardia-Laguarta, C., Velasco, K.R., Area-Gomez, E., Dal Bello, F., De Stefani, D. *et al.* (2019) MFN2 mutations in Charcot-Marie-Tooth disease alter mitochondria-associated ER membrane function but do not impair bioenergetics. *Hum. Mol. Genet.*, **28**, 1782–1800.
42. Misko, A., Jiang, S., Wegorzewska, I., Milbrandt, J. and Baloh, R.H. (2010) Mitofusin 2 is necessary for transport of axonal mitochondria and interacts with the Miro/Milton complex. *J. Neurosci.*, **30**, 4232–4240.
43. Rocha, A.G., Franco, A., Krezel, A.M., Rumsey, J.M., Alberti, J.M., Knight, W.C., Biris, N., Zacharioudakis, E., Janetka, J.W., Baloh, R.H. *et al.* (2018) MFN2 agonists reverse mitochondrial defects in preclinical models of Charcot-Marie-Tooth disease type 2A. *Science*, **360**, 336–341.
44. Rizzo, F., Ronchi, D., Salani, S., Nizzardo, M., Fortunato, F., Bordoni, A., Stuppia, G., Del Bo, R., Piga, D., Fato, R. *et al.* (2016) Selective mitochondrial depletion, apoptosis resistance, and increased mitophagy in human Charcot-Marie-Tooth 2A motor neurons. *Hum. Mol. Genet.*, **25**, 4266–4281.
45. Dorn, G.W. (2020) Mitofusin 2 dysfunction and disease in mice and men. *Front. Physiol.*, **11**, 782.

46. Zhao, T., Huang, X., Han, L., Wang, X., Cheng, H., Zhao, Y., Chen, Q., Chen, J., Cheng, H., Xiao, R. *et al.* (2012) Central role of mitofusin 2 in autophagosome-lysosome fusion in cardiomyocytes. *J. Biol. Chem.*, **287**, 23615–23625.
47. Sebastián, D. and Zorzano, A. (2016) When MFN2 (mitofusin 2) met autophagy: a new age for old muscles. *Autophagy*, **12**, 2250–2251.
48. Peng, C., Rao, W., Zhang, L., Gao, F., Hui, H., Wang, K., Dai, S., Yang, Y., Luo, P., Ma, Y. *et al.* (2018) Mitofusin 2 exerts a protective role in ischemia reperfusion injury through increasing autophagy. *Cell. Physiol. Biochem.*, **46**, 2311–2324.
49. Neufeld, T.P. (2012) Autophagy and cell growth – the yin and yang of nutrient responses. *J. Cell Sci.*, **125**, 2359–2368.
50. Hardie, D.G. (2007) AMP-activated/SNF1 protein kinases: conserved guardians of cellular energy. *Nat. Rev. Mol. Cell Biol.*, **8**, 774–785.
51. Samuels, Y., Wang, Z., Bardelli, A., Silliman, N., Ptak, J., Szabo, S., Yan, H., Gazdar, A., Powell, S.M., Riggins, G.J. *et al.* (2004) High frequency of mutations of the PIK3CA gene in human cancers. *Science*, **304**, 554–554.
52. Shaw, R.J. and Cantley, L.C. (2006) Ras, PI(3)K and mTOR signalling controls tumour cell growth. *Nature*, **441**, 424–430.
53. Nazio, F. and Cecconi, F. (2017) Autophagy up and down by outsmarting the incredible ULK. *Autophagy*, **13**, 967–968.
54. Levine, B. and Kroemer, G. (2008) Autophagy in the pathogenesis of disease. *Cell*, **132**, 27–42.
55. Galluzzi, L., Pietrocola, F., Bravo-San Pedro, J.M., Amaravadi, R.K., Baehrecke, E.H., Cecconi, F., Codogno, P., Debnath, J., Gewirtz, D.A., Karantza, V. *et al.* (2015) Autophagy in malignant transformation and cancer progression. *EMBO J.*, **34**, 856–880.
56. White, E. (2012) Deconvoluting the context-dependent role for autophagy in cancer. *Nat. Rev. Cancer*, **12**, 401–410.
57. Xue, R., Meng, Q., Lu, D., Liu, X., Wang, Y. and Hao, J. (2018) Mitofusin2 induces cell autophagy of pancreatic cancer through inhibiting the PI3K/Akt/mTOR signaling pathway. *Oxidative Med. Cell. Longev.*, **2018**, 2798070.
58. Berti, B., Longo, G., Mari, F., Doccini, S., Piccolo, I., Donati, M.A., Moro, F., Guerrini, R., Santorelli, F.M. and Petruzzella, V. (2021) Bi-allelic variants in MTMR5/SBF1 cause Charcot-Marie-Tooth type 4B3 featuring mitochondrial dysfunction. *BMC Med. Genet.*, **14**, 157.
59. Richards, S., Aziz, N., Bale, S., Bick, D., Das, S., Gastier-Foster, J., Grody, W.W., Hegde, M., Lyon, E., Spector, E. *et al.* (2015) Standards and guidelines for the interpretation of sequence variants: a joint consensus recommendation of the American College of Medical Genetics and Genomics and the Association for Molecular Pathology. *Genet. Med.*, **17**, 405–424.
60. Xie, Y., Li, X., Liu, L., Hu, Z., Huang, S., Zhan, Y., Zi, X., Xia, K., Tang, B. and Zhang, R. (2016) MFN2-related genetic and clinical features in a cohort of Chinese CMT2 patients. *J. Peripher. Nerv. Syst.*, **21**, 38–44.
61. Chen, H., Detmer, S.A., Ewald, A.J., Griffin, E.E., Fraser, S.E. and Chan, D.C. (2003) Mitofusins Mfn1 and Mfn2 coordinately regulate mitochondrial fusion and are essential for embryonic development. *J. Cell Biol.*, **160**, 189–200.
62. Filadi, R., Greotti, E., Turacchio, G., Luini, A., Pozzan, T. and Pizzo, P. (2015) Mitofusin 2 ablation increases endoplasmic reticulum-mitochondria coupling. *Proc. Natl. Acad. Sci. U. S. A.*, **112**, E2174–E2181.
63. Rouzier, C., Bannwarth, S., Chaussenot, A., Chevrollier, A., Verschueren, A., Bonello-Palot, N., Fragaki, K., Cano, A., Pouget, J., Pellissier, J.-F. *et al.* (2012) The MFN2 gene is responsible for mitochondrial DNA instability and optic atrophy "plus" phenotype. *Brain*, **135**, 23–34.
64. Verhoeven, K., Claeys, K.G., Züchner, S., Schröder, J.M., Weis, J., Ceuterick, C., Jordanova, A., Nelis, E., De Vriendt, E., Van Hul, M. *et al.* (2006) MFN2 mutation distribution and genotype/phenotype correlation in Charcot-Marie-Tooth type 2. *Brain*, **129**, 2093–2102.
65. Delettre, C., Lenaers, G., Griffoin, J.-M., Gigarel, N., Lorenzo, C., Belenguer, P., Pelloquin, L., Grosgeorge, J., Turc-Carel, C., Perret, E. *et al.* (2000) Nuclear gene OPA1, encoding a mitochondrial dynamin-related protein, is mutated in dominant optic atrophy. *Nat. Genet.*, **26**, 207–210.
66. Ishihara, N., Fujita, Y., Oka, T. and Mihara, K. (2006) Regulation of mitochondrial morphology through proteolytic cleavage of OPA1. *EMBO J.*, **25**, 2966–2977.
67. Anand, R., Langer, T. and Baker, M.J. (2013) Proteolytic control of mitochondrial function and morphogenesis. *Biochim. Biophys. Acta (BBA) – Mol. Cell Res.*, **1833**, 195–204.
68. Otera, H., Wang, C., Cleland, M.M., Setoguchi, K., Yokota, S., Youle, R.J. and Mihara, K. (2010) Mff is an essential factor for mitochondrial recruitment of Drp1 during mitochondrial fission in mammalian cells. *J. Cell Biol.*, **191**, 1141–1158.
69. Lin, X.-H., Qiu, B.-Q., Ma, M., Zhang, R., Hsu, S.-J., Liu, H.-H., Chen, J., Gao, D.-M., Cui, J.-F., Ren, Z.-G. *et al.* (2020) Suppressing DRP1-mediated mitochondrial fission and mitophagy increases mitochondrial apoptosis of hepatocellular carcinoma cells in the setting of hypoxia. *Oncogene*, **9**, 67.
70. Hu, C., Huang, Y. and Li, L. (2017) Drp1-dependent mitochondrial fission plays critical roles in physiological and pathological progresses in mammals. *Int. J. Mol. Sci.*, **18**, E144.
71. Ranieri, M., Brajkovic, S., Riboldi, G., Ronchi, D., Rizzo, F., Bresolin, N., Corti, S. and Comi, G.P. (2013) Mitochondrial fusion proteins and human diseases. *Neurol. Res. Int.*, **2013**, 1–11.
72. Glancy, B., Willis, W.T., Chess, D.J. and Balaban, R.S. (2013) Effect of calcium on the oxidative phosphorylation cascade in skeletal muscle mitochondria. *Biochemistry*, **52**, 2793–2809.
73. Llorente-Folch, I., Rueda, C.B., Pardo, B., Szabadkai, G., Duchen, M.R. and Satrustegui, J. (2015) The regulation of neuronal mitochondrial metabolism by calcium. *J. Physiol.*, **593**, 3447–3462.
74. Pich, S., Bach, D., Briones, P., Liesa, M., Camps, M., Testar, X., Palacín, M. and Zorzano, A. (2005) The Charcot-Marie-Tooth type 2A gene product, Mfn2, up-regulates fuel oxidation through expression of OXPHOS system. *Hum. Mol. Genet.*, **14**, 1405–1415.
75. Parzych, K.R. and Klionsky, D.J. (2014) An overview of autophagy: morphology, mechanism, and regulation. *Antioxid. Redox Signal.*, **20**, 460–473.
76. Katsuragi, Y., Ichimura, Y. and Komatsu, M. (2015) p62/SQSTM1 functions as a signaling hub and an autophagy adaptor. *FEBS J.*, **282**, 4672–4678.
77. Klionsky, D.J., Abdel-Aziz, A.K., Abdelfatah, S., Abdellatif, M., Abdoli, A., Abel, S., Abeliovich, H., Abildgaard, M.H., Abudu, Y.P., Acevedo-Arozena, A. *et al.* (2021) Guidelines for the use and interpretation of assays for monitoring autophagy (4th edition). *Autophagy*, **17**, 1–382.
78. Szklarczyk, D., Franceschini, A., Wyder, S., Forslund, K., Heller, D., Huerta-Cepas, J., Simonovic, M., Roth, A., Santos, A., Tsafou, K.P. *et al.* (2015) STRING v10: protein–protein interaction networks, integrated over the tree of life. *Nucleic Acids Res.*, **43**, D447–D452.

79. Doncheva, N.T., Morris, J.H., Gorodkin, J. and Jensen, L.J. (2019) Cytoscape StringApp: network analysis and visualization of proteomics data. *J. Proteome Res.*, **18**, 623–632.
80. Bordi, M., De Cegli, R., Testa, B., Nixon, R.A., Ballabio, A. and Cecconi, F. (2021) A gene toolbox for monitoring autophagy transcription. *Cell Death Dis.*, **12**, 1044.
81. Seto, S., Sugaya, K., Tsujimura, K., Nagata, T., Horii, T. and Koide, Y. (2013) Rab39a interacts with phosphatidylinositol 3-kinase and negatively regulates autophagy induced by lipopolysaccharide stimulation in macrophages. *PLoS One*, **8**, e83324.
82. Niu, M., Zheng, N., Wang, Z., Gao, Y., Luo, X., Chen, Z., Fu, X., Wang, Y., Wang, T., Liu, M. *et al.* (2020) RAB39B deficiency impairs learning and memory partially through compromising autophagy. *Front. Cell Dev. Biol.*, **8**, 598622.
83. Koss, D.J., Campesan, S., Giorgini, F. and Outeiro, T.F. (2021) Dysfunction of RAB39B- mediated vesicular trafficking in Lewy body diseases. *Mov. Disord.*, **36**, 1744–1758.
84. Yu, J.S.L. and Cui, W. (2016) Proliferation, survival and metabolism: the role of PI3K/AKT/mTOR signalling in pluripotency and cell fate determination. *Development*, **143**, 3050–3060.
85. Burgering, B.M. and Coffer, P.J. (1995) Protein kinase B (c-Akt) in phosphatidylinositol-3-OH kinase signal transduction. *Nature*, **376**, 599–602.
86. Sarbassov, D.D., Guertin, D.A., Ali, S.M. and Sabatini, D.M. (2005) Phosphorylation and regulation of Akt/PKB by the Rictor-mTOR complex. *Science*, **307**, 1098–1101.
87. Sarbassov, D.D., Ali, S.M., Sengupta, S., Sheen, J.-H., Hsu, P.P., Bagley, A.F., Markhard, A.L. and Sabatini, D.M. (2006) Prolonged rapamycin treatment inhibits mTORC2 assembly and Akt/PKB. *Mol. Cell*, **22**, 159–168.
88. Hresko, R.C. and Mueckler, M. (2005) mTOR·RICTOR is the Ser473 kinase for Akt/protein kinase B in 3T3-L1 adipocytes. *J. Biol. Chem.*, **280**, 40406–40416.
89. Matheny, R.W. and Adamo, M.L. (2009) Current perspectives on Akt Akt-ivation and Akt-ions. *Exp. Biol. Med. (Maywood)*, **234**, 1264–1270.
90. Krześlak, A. (2010) Akt kinase: a key regulator of metabolism and progression of tumors. *Postepy Hig. Med. Dosw. (Online)*, **64**, 490–503.
91. Filadi, R., Pendin, D. and Pizzo, P. (2018) Mitofusin 2: from functions to disease. *Cell Death Dis.*, **9**, 330.
92. Chen, H. and Chan, D.C. (2006) Critical dependence of neurons on mitochondrial dynamics. *Curr. Opin. Cell Biol.*, **18**, 453–459.
93. Pareyson, D., Saveri, P., Sagnelli, A. and Piscosquito, G. (2015) Mitochondrial dynamics and inherited peripheral nerve diseases. *Neurosci. Lett.*, **596**, 66–77.
94. Crunkhorn, S. (2018) Rescuing mitochondrial motility. *Nat. Rev. Drug Discov.*, **17**, 391–391.
95. Saporta, M.A., Dang, V., Volfson, D., Zou, B., Xie, X.S., Adebola, A., Liem, R.K., Shy, M. and Dimos, J.T. (2015) Axonal Charcot-Marie-Tooth disease patient-derived motor neurons demonstrate disease-specific phenotypes including abnormal electrophysiological properties. *Exp. Neurol.*, **263**, 190–199.
96. Cartoni, R., Léger, B., Hock, M.B., Praz, M., Crettenand, A., Pich, S., Ziltener, J.-L., Luthi, F., Dériaz, O., Zorzano, A. *et al.* (2005) Mitofusins 1/2 and ERRα expression are increased in human skeletal muscle after physical exercise: mitofusins 1/2 and ERRα expression in skeletal muscle. *J. Physiol.*, **567**, 349–358.
97. Mourier, A., Motori, E., Brandt, T., Lagouge, M., Atanassov, I., Galinier, A., Rappl, G., Brodesser, S., Hultenby, K., Dieterich, C. *et al.* (2015) Mitofusin 2 is required to maintain mitochondrial coenzyme Q levels. *J. Cell Biol.*, **208**, 429–442.
98. Short, B. (2015) Mitofusin 2 keeps the respiratory chain on Q. *J. Cell Biol.*, **208**, 382–382.
99. Morán, M., Delmiro, A., Blázquez, A., Ugalde, C., Arenas, J. and Martín, M.A. (2014) Bulk autophagy, but not mitophagy, is increased in cellular model of mitochondrial disease. *Biochim. Biophys. Acta (BBA) - Mol. Basis Dis.*, **1842**, 1059–1070.
100. Xiong, W., Ma, Z., An, D., Liu, Z., Cai, W., Bai, Y., Zhan, Q., Lai, W., Zeng, Q., Ren, H. *et al.* (2019) Mitofusin 2 participates in mitophagy and mitochondrial fusion against angiotensin II-induced cardiomyocyte injury. *Front. Physiol.*, **10**, 411.
101. Stavoe, A.K.H. and Holzbaur, E.L.F. (2019) Axonal autophagy: mini-review for autophagy in the CNS. *Neurosci. Lett.*, **697**, 17–23.
102. Guo, F., Liu, X., Cai, H. and Le, W. (2018) Autophagy in neurodegenerative diseases: pathogenesis and therapy: autophagy in neurodegenerative diseases. *Brain Pathol.*, **28**, 3–13.
103. Song, Y., Shang, D., Cheng, H. and Zhou, R. (2018) The small GTPase RAB37 functions as an organizer for autophagosome biogenesis. *Autophagy*, **14**, 727–729.
104. Hayashi-Nishino, M., Fujita, N., Noda, T., Yamaguchi, A., Yoshimori, T. and Yamamoto, A. (2009) A subdomain of the endoplasmic reticulum forms a cradle for autophagosome formation. *Nat. Cell Biol.*, **11**, 1433–1437.
105. Axe, E.L., Walker, S.A., Manifava, M., Chandra, P., Roderick, H.L., Habermann, A., Griffiths, G. and Ktistakis, N.T. (2008) Autophagosome formation from membrane compartments enriched in phosphatidylinositol 3-phosphate and dynamically connected to the endoplasmic reticulum. *J. Cell Biol.*, **182**, 685–701.
106. Cartoni, R. and Martinou, J.-C. (2009) Role of mitofusin 2 mutations in the physiopathology of Charcot-Marie-Tooth disease type 2A. *Exp. Neurol.*, **218**, 268–273.
107. Hailey, D.W., Rambold, A.S., Satpute-Krishnan, P., Mitra, K., Sougrat, R., Kim, P.K. and Lippincott-Schwartz, J. (2010) Mitochondria supply membranes for autophagosome biogenesis during starvation. *Cell*, **141**, 656–667.
108. McEwan, D.G. and Dikic, I. (2010) Not all autophagy membranes are created equal. *Cell*, **141**, 564–566.
109. Hamasaki, M., Furuta, N., Matsuda, A., Nezu, A., Yamamoto, A., Fujita, N., Oomori, H., Noda, T., Haraguchi, T., Hiraoka, Y. *et al.* (2013) Autophagosomes form at ER-mitochondria contact sites. *Nature*, **495**, 389–393.
110. Wei, H., Liu, L. and Chen, Q. (2015) Selective removal of mitochondria via mitophagy: distinct pathways for different mitochondrial stresses. *Biochim. Biophys. Acta (BBA) – Mol. Cell Res.*, **1853**, 2784–2790.
111. Villanueva Paz, M., Cotán, D., Garrido-Maraver, J., Cordero, M.D., Oropesa-Ávila, M., de La Mata, M., Delgado Pavón, A., de Lavera, I., Alcocer-Gómez, E. and Sánchez-Alcázar, J.A. (2016) Targeting autophagy and mitophagy for mitochondrial diseases treatment. *Expert Opin. Ther. Targets*, **20**, 487–500.
112. Dorn, G.W. (2016) Parkin-dependent mitophagy in the heart. *J. Mol. Cell. Cardiol.*, **95**, 42–49.
113. Pickles, S., Vigié, P. and Youle, R.J. (2018) Mitophagy and quality control mechanisms in mitochondrial maintenance. *Curr. Biol.*, **28**, R170–R185.
114. Lee, H.J., Jang, S.H., Kim, H., Yoon, J.H. and Chung, K.C. (2012) PINK1 stimulates interleukin-1β-mediated inflammatory signaling via the positive regulation of TRAF6 and TAK1. *Cell. Mol. Life Sci.*, **69**, 3301–3315.
115. Chen, Y. and Dorn, G.W. (2013) PINK1-phosphorylated mitofusin 2 is a Parkin receptor for culling damaged mitochondria. *Science*, **340**, 471–475.

116. Chen, B.B., Coon, T.A., Glasser, J.R., Zou, C., Ellis, B., Das, T., McKelvey, A.C., Rajbhandari, S., Lear, T., Kamga, C. *et al.* (2014) E3 ligase subunit Fbxo15 and PINK1 kinase regulate cardiolipin synthase 1 Stability and mitochondrial function in pneumonia. *Cell Rep.*, **7**, 476–487.
117. Song, M., Gong, G., Burelle, Y., Gustafsson, Å.B., Kitsis, R.N., Matkovich, S.J. and Dorn, G.W. (2015) Interdependence of parkin-mediated mitophagy and mitochondrial fission in adult mouse hearts. *Circ. Res.*, **117**, 346–351.
118. Song, M., Franco, A., Fleischer, J.A., Zhang, L. and Dorn, G.W. (2017) Abrogating mitochondrial dynamics in mouse hearts accelerates mitochondrial senescence. *Cell Metab.*, **26**, 872–883.e5.
119. Sarraf, S.A., Raman, M., Guarani-Pereira, V., Sowa, M.E., Huttlin, E.L., Gygi, S.P. and Harper, J.W. (2013) Landscape of the PARKIN-dependent ubiquitylome in response to mitochondrial depolarization. *Nature*, **496**, 372–376.
120. Mostowy, S. (2014) Multiple roles of the cytoskeleton in bacterial autophagy. *PLoS Pathog.*, **10**, e1004409.
121. Wang, R.C., Wei, Y., An, Z., Zou, Z., Xiao, G., Bhagat, G., White, M., Reichelt, J. and Levine, B. (2012) Akt-mediated regulation of autophagy and tumorigenesis through Beclin 1 phosphorylation. *Science*, **338**, 956–959.
122. Ballesteros-Álvarez, J. and Andersen, J.K. (2021) mTORC2: the other mTOR in autophagy regulation. *Aging Cell*, **20**, e13431. 1–17.
123. Wang, S. and Gu, K. (2017) Insulin-like growth factor 1 inhibits autophagy of human colorectal carcinoma drug-resistant cells via the protein kinase B/mammalian target of rapamycin signaling pathway. *Mol. Med. Rep.*, **17**, 2952–2956.
124. Marsboom, G., Toth, P.T., Ryan, J.J., Hong, Z., Wu, X., Fang, Y.-H., Thenappan, T., Piao, L., Zhang, H.J., Pogoriler, J. *et al.* (2012) Dynamin-related protein 1-mediated mitochondrial mitotic fission permits hyperproliferation of vascular smooth muscle cells and offers a novel therapeutic target in pulmonary hypertension. *Circ. Res.*, **110**, 1484–1497.
125. Ranieri, C., Di Tommaso, S., Loconte, D.C., Grossi, V., Sanese, P., Bagnulo, R., Susca, F.C., Forte, G., Peserico, A., De Luisi, A. *et al.* (2018) In vitro efficacy of ARQ 092, an allosteric AKT inhibitor, on primary fibroblast cells derived from patients with PIK3CA-related overgrowth spectrum (PROS). *Neurogenetics*, **19**, 77–91.
126. Zoccolella, S., Artuso, L., Capozzo, R., Amati, A., Guerra, F., Simone, I., Logroscino, G. and Petruzzella, V. (2012) Mitochondrial genome large rearrangements in the skeletal muscle of a patient with PMA. *Eur. J. Neurol.*, **19**, e63–e64.
127. Bianco, A., Valletti, A., Longo, G., Bisceglia, L., Montoya, J., Emperador, S., Guerriero, S. and Petruzzella, V. (2018) Mitochondrial DNA copy number in affected and unaffected LHON mutation carriers. *BMC. Res. Notes*, **11**, 911.
128. Duan, S., Hajek, P., Lin, C., Shin, S.K., Attardi, G. and Chomyn, A. (2003) Mitochondrial outer membrane permeability change and hypersensitivity to digitonin early in staurosporine-induced apoptosis. *J. Biol. Chem.*, **278**, 1346–1353.
129. Pezzini, I., Marino, A., Del Turco, S., Nesti, C., Doccini, S., Cappello, V., Gemmi, M., Parlanti, P., Santorelli, F.M., Mattoli, V. *et al.* (2017) Cerium oxide nanoparticles: the regenerative redox machine in bioenergetic imbalance. *Nanomedicine*, **12**, 403–416.
130. Chazotte, B. (2011) Labeling mitochondria with JC-1. *Cold Spring Harb Protoc*, **2011**, pdb.prot065490.
131. Akram, K.M. (2013) Idiopathic pulmonary fibrosis: exploration of aberrant epithelial wound repair and stem cell-mediated regenerative approaches.
132. Chen, S., Zhou, Y., Chen, Y. and Gu, J. (2018) fastp: an ultra-fast all-in-one FASTQ preprocessor. *Bioinformatics*, **34**, i884–i890.
133. Dobin, A., Davis, C.A., Schlesinger, F., Drenkow, J., Zaleski, C., Jha, S., Batut, P., Chaisson, M. and Gingeras, T.R. (2013) STAR: ultrafast universal RNA-seq aligner. *Bioinformatics*, **29**, 15–21.
134. Szklarczyk, D., Morris, J.H., Cook, H., Kuhn, M., Wyder, S., Simonovic, M., Santos, A., Doncheva, N.T., Roth, A., Bork, P. *et al.* (2017) The STRING database in 2017: quality-controlled protein–protein association networks, made broadly accessible. *Nucleic Acids Res.*, **45**, D362–D368.